Regular and chaotic advection in the flow field of a three-vortex system

Leonid Kuznetsov[1] and George M. Zaslavsky[1,2]
[1]*Department of Physics, New York University, 2-4 Washington Place, New York, New York 10003*
[2]*Courant Institute of Mathematical Sciences, New York University, 251 Mercer Street, New York, New York 10012*
(Received 7 May 1998)

The dynamics of a passive particle in a two-dimensional incompressible flow generated by three point vortices advected by their mutual interaction is considered as a periodically forced Hamiltonian system. The geometry of the background vortex flow determines the degree of chaotization of the tracer motion. Two extreme regimes, of strong and weak chaos, are specified and investigated analytically. Mappings are derived for both cases, and the border between the chaotic and regular advection is found by applying the stochasticity criterion. In the case of strong chaos, there exist coherent regular structures around vortices (vortex cores), which correspond to domains with *KAM* curves. An expression for the radius of the cores is obtained. The robust nature of vortex cores, demonstrated numerically, is explained. In the near-integrable case of weak chaotization, a separatrix map is used to find the width of the stochastic layer. Numerical simulations reveal a variety of structures in the pattern of advection, such as a hierarchy of island chains and sticky bands around the vortex cores. [S1063-651X(98)03612-5]

PACS number(s): 47.32.Cc, 47.52.+j, 05.45.+b

I. INTRODUCTION

The motion of small particles in flows, known as advection, has been related in many recent publications to such areas as fluid stirring, chemical reactions, pollution of the atmosphere and the ocean, visualization of flows, etc. Speaking about a small particle, we have in mind a particle that does not influence the flow. Other terms are sometimes used, such as tracers, passive particles, or Lagrangian particles. For cases when the flow is stationary, incompressible, and inviscid, an advected particle trajectory coincides with the streamline of the flow, and the information obtained from the advection describes the structure of the flow. The general form of the advection equation is

$$\dot{\mathbf{r}} = \mathbf{v}(\mathbf{r},t), \tag{1.1}$$

where $\mathbf{r}$ is a coordinate vector of the particle, and $\mathbf{v}$ is a given velocity field which defines the flow. Formally, Eq. (1.1) describes a dynamical system which, generally speaking, possesses chaotic solutions for some parameter values and initial conditions. In this case the advection is known as chaotic. The notion of Lagrangian turbulence is also used for chaotic solutions of Eq. (1.1). Chaotic advection has been observed in numerous experiments and computer simulations, and a number of different theoretical descriptions have been published (see, for example, Refs. [1–10], which represent only a small part of the actual list of important publications).

For a divergence-free velocity field ($\mathrm{div}\,\mathbf{v}=0$), system (1.1) can be written in Hamiltonian form. This form is known explicitly for the three-dimensional stationary case $\mathbf{v}=\mathbf{v}(x,y,z)$, and for two-dimensional generic case $\mathbf{v}=\mathbf{v}(x,y,t)$, when Eq. (1.1) can be rewritten as

$$\dot{x} = v_x(x,y,t) = \partial\Psi/\partial y, \qquad \dot{y} = v_y(x,y,t) = -\partial\Psi/\partial x, \tag{1.2}$$

using the stream function $\Psi=\Psi(x,y,t)$ that plays the role of a Hamiltonian. Both the above mentioned cases belong to so-called Hamiltonian systems with $1\frac{1}{2}$ degrees of freedom. Such a Hamiltonian system possesses chaotic advection for some domains of the phase space, which is simply an (x,y) plane for case (1.2).

Application of the methods of the dynamical system theory to the chaotic advection problem has become an established technique. By now chaotization of the tracer motion has been observed and studied in a large number of systems, including point vortex flows [11–14], Rayleigh-Bénard convection [15,16], blinking vortices [1], an oscillating vortex pair [5,6], and a vortex pair perturbed by another point vortices [17], point vortex flows in bounded domains [18–20], etc. We want to emphasize that the correspondence of a trajectory of an advected particle in physical (coordinate) space to the phase-space trajectory of a Hamiltonian system implies more than just the appearance of Lagrangian chaos in a generic unsteady velocity field. One should also expect the configuration space of a tracer to contain all the typical structures of Hamiltonian phase space, such as islands of regular motion around elliptic points, cantori, hierarchy of island chains, thin stochastic layers inside the islands, etc. In fact, such structures were observed in a number of works devoted to the chaotic advection in the time-periodic flows, where the possibility of constructing a Poincaré map for the tracer motion provides us with a convenient visualization technique [5,18–22]. The importance of this observation is due to the crucial role of these objects for the transport process. For Hamiltonian systems with $1\frac{1}{2}$ degrees of freedom, one can establish connections between the topology of the phase space and the properties of transport [23], which makes a detailed study of the phase space topology more significant.

Point vortex flows, a singular solutions of the two-dimensional (2D) Euler equation, are one of the most natural and most frequently addressed examples of velocity fields, generating the Lagrangian chaos of the tracers. A traditional

subject matter of fluid mechanics for over a hundred years, (see Refs. [24–26] for a review), point vortex systems, on the one hand, share certain features with the more involved case of coherent vortex structures in 2D turbulence [27–31], and, on the other hand can be regarded as Hamiltonian systems with few degrees of freedom; thus not only the advection, but the dynamics of the flow itself (in a Lagrangian framework), can be attacked by the machinery of the Hamiltonian dynamics.

The motion of a passive particle in a three point vortex system, sometimes called the restricted four-vortex problem due to its analogy to the restricted three-body problem in celestial mechanics [13], is one of the oldest examples of 2D chaotic advection. It is worthwhile to mention here that the nonintegrability of the general four-vortex system was established in Ref. [32], and further discussed in Refs. [33,34]. The nonintegrability of the equations for tracer trajectories in the field of three vortices, and the existence of chaotic motion in this system, were demonstrated numerically in Ref. [11], and analytically, using the Melnikov method [35], in Ref. [12], actually before the term chaotic advection established itself.

In Sec. II the governing dynamical equations are specified. In the case of a three point vortex system, the flow part of the dynamics is integrable, and the velocity field can be found in an explicit form. We write the solution for the vortex trajectories, and give a brief review of the types of vortex motion.

The integrability of the underlying vortex motion makes it possible to carry out a detailed analytical study of the advection. In Sec. III, we consider the case of strong chaotization of the tracer motion. We apply the traditional tools of chaotic dynamics to the problem of the coherent vortex cores—the areas of regular advection around vortices. The appearance of nonmixing patches is by far not limited to point vortex flows; in fact, these constitute a robust feature of practically any flow with regions of concentrated vorticity [27–30,36–39]. The comparative numerical study of advection in point vortex systems and in 2D turbulence carried out in Ref. [27] revealed certain common features of advection patterns in these two cases. Point vortex models have enormous advantages for an analytical treatment of the tracer motion, and in particular, for a study of coherent cores. These advantages stem from the fact that the vortices themselves are advected by the flow and thus, as we already mentioned, their motion can be described via Hamiltonian equations. The appropriate dynamical variable for the problem of a tracer moving coherently with the vortex is the displacement of the tracer from the vortex; in other words, the coordinates of the tracer in the moving vortex reference frame. It is clear that the equations governing the dynamics of the displacement will be Hamiltonian, since those for both vortex and tracer are. The possibility to study the problem completely explains the origin of the near-vortex isolated nonpenetrable core. Its specific structure possesses a level of universality which can be efficiently used for a tracer dynamics in the multivortex system. The existence of the cores as coherent structures can be utilized for speculations on 2D vortex turbulence, since each vortex can be considered as an advected particle in a many-vortex system. Using the equations in the moving vortex frame, we construct a mapping for the trajectories of the tracer inside the coherent core. Applying the stochasticity criterion to this map, (see Refs. [10,40] concerning chaos in area-preserving maps), we obtain the analytic expression for the radius of the coherent core, which is in a good agreement with numerical results.

In Sec. IV, we address the case when the vortex motion is close to a steady rotating equilateral triangle configuration. The motion of the tracer is chaotic only inside the thin layer around the destructed separatrices of the integrable ''equilateral'' case. The Melnikov method, used in Ref. [12] to prove the nonintegrability of a restricted four-vortex problem, also allows one to obtain the width of the stochastic layers in the case of weak chaotization. To do this, the separatrix map [41,10] for the tracer motion is constructed.

Numerical studies in Refs. [13,27] demonstrated the existence of coherent cores around the vortices, with a sharp border between regular and chaotic regions. In Ref. [13], different regimes of advection were simulated, and Poincaré sections of the tracer trajectories were constructed to visualize the geometry of the mixing region. In Sec. V, we present a more detailed description of the structures in the advection pattern, paying special attention to the boundaries between the areas of chaotic and regular motion. Apart from typical sticky island hierarchies on the border of islands around elliptic points, we have found that, for certain geometries of the vortex motion, the boundaries of the regular cores surrounding vortices contain a complex mingling of small, extremely elongated islands, that create strong stickiness.

II. DYNAMICAL EQUATIONS

Point vortex flows are singular solutions of the 2D Euler equation, and Helmholtz's vorticity theorems allow one to reduce the dynamics of such a flow to a Hamiltonian system with N degrees of freedom, where N is the number of vortices. We denote the coordinates of the vortices in the plane as x_m and y_m, and their strengths as k_m. It is convenient to introduce complex coordinate: $z=x+iy$, and to specify the positions of the vortices by means of complex-valued functions of time: $z_m(t)=x_m(t)+iy_m(t)$, $m=1,\ldots,N$. Then, for the unbounded domain, the motion of the vortices will be governed by the equations [42,34]

$$\dot{z}_m^*=\frac{1}{2\pi i}\sum_{j\neq m}\frac{k_j}{z_m-z_j} \quad (m,j=1,\ldots,N). \tag{2.1}$$

Below we consider the system of three-point vortices of equal strength $k\equiv k_m$, $m=1$, 2, and 3. The dynamics of three-point vortices was studied extensively by several authors, and by now we have a complete description of motion types for arbitrary vortex strengths [43–46]. For the convenience of our readers, we will briefly outline the solution of Eq. (2.1) for the case of three identical vortices, following the method of Ref. [34]. For vortices of different strength, in order to put Eq. (2.1) into Hamiltonian form, physical coordinates should be rescaled, which can be done in different ways; see for example, Refs. [14,34,47]. In the case of identical vortices, canonical coordinates coincide with the physical coordinates in the plane, and Eqs. (2.1) have a Hamiltonian form:

$$\dot{z}_m^* = [z_m^*, H] = \frac{k}{2\pi i} \sum_{j \neq m} \frac{1}{z_m - z_j} \quad (m, j = 1,2,3), \tag{2.2}$$

with a Hamiltonian function

$$H = -\frac{k}{4\pi} \sum_{j \neq m} \ln|z_m - z_j|^2 \tag{2.3}$$

and fundamental Poisson bracket

$$[z_m, z_j] = 0, \quad [z_m, z_j^*] = -2i\delta_{mj}. \tag{2.4}$$

As a result of translational and rotational invariance of the Hamiltonian (2.3), vortex ''momentum''

$$Q + iP \equiv \sum_{j=1}^{3} z_j \tag{2.5}$$

and ''angular momentum''

$$L^2 \equiv \sum_{j=1}^{3} |z_j|^2 \tag{2.6}$$

are conserved during the motion. Using Eq. (2.4), one can form three integrals in involution for system (2.2); they are H, L^2, and $Q^2 + P^2$. Thus the Liouville theorem guarantees the integrability of Eq. (2.2). Components of the vortex momentum Q and P define the coordinates of the center of vorticity, and below, by placing the origin of coordinate system in this point, we will put $Q = P = 0$. With this choice of the coordinate origin, L^2 equals to the average squared distance between the vortices:

$$L^2 = \tfrac{1}{3} \sum_{j>m} |z_j - z_m|^2 \quad (j, m = 1,2,3). \tag{2.7}$$

This defines the spatial scale of the motion, and can be made equal to 1 by an appropriate rescaling of coordinates $z \to z/L$. The vortex strength k also can be scaled out by redefining the time variable: $t \to (k/L^2)t$. The only parameter that distinguishes different types of motion is the value of the Hamiltonian H, which can be related to the geometry of the vortex configuration, e.g., to the product of side lengths of the vortex triangle Λ:

$$e^{-2\pi H} = \Lambda \equiv |z_1 - z_2||z_2 - z_3||z_3 - z_1|, \tag{2.8}$$

written in the dimensionless form with $k = L = 1$. These parameters vary from $H = 0$ and $\Lambda = 1$, when vortices stay in the vertices of uniformly rotating equilateral triangle, up to the limiting values $H = \infty$ and $\Lambda = 0$, when two of the three vortices coalesce.

It is shown in Appendix A how system (2.1) can be reduced to Eq. (A19) for the ''area variable'' $I(t)$, proportional to the square of the area of the triangle spanned by vortices [see definition (A17)], and eventually, solved in quadratures. The solution has the form

$$z_m(t) = 6^{-1/2} L e^{i\phi_2/2} [(1 - I^{1/2})^{1/2} e^{-2\pi i(m-1)/3} e^{-i\phi_1/2} + (1 + I^{1/2})^{1/2} e^{-4\pi i(m-1)/3} e^{i\phi_1/2}], \quad m = 1,2,3, \tag{2.9}$$

with expressions for $I(t)$, $\phi_1(t)$, and $\phi_2(t)$ given in Appendix A [formulas (A24), (A30), and (A32)]. This form will be used in Secs. III and IV to find the domains of regular and chaotic advection of the flow produced by three vortices.

The relative motion of vortices is described by the term in square brackets in Eq. (2.9), and is periodic for any Λ except for the separatrix case $\Lambda = \Lambda_c \equiv 1/\sqrt{2}$ [see Eq. (A24)]; its period $T_{\rm rel}$ is given by Eq. (A29). Characteristic features of the two types of relative motion ($\Lambda > \Lambda_c$ and $\Lambda < \Lambda_c$) are described in considerable detail in Refs. [43,26]. We point out, that, for the ''triangular'' case, $\Lambda > \Lambda_c$, the vortex configuration oscillates between two isosceles triangles—an acute one, when the area of the triangle reaches its maximum; and an obtuse one with minimum area. During one period of relative motion, each of these shapes is repeated three times, corresponding to three different cyclic permutations of vortices in the vertices of the triangle. Vortices never reach a collinear configuration, and the orientation of vortex triangle σ, defined as $\sigma = +1$ for the counterclockwise arrangement of vortices 1, 2, and 3 along the perimeter of the vortex triangle, and $\sigma = -1$ for the clockwise arrangement does not change during the motion. All three vortices are equivalent; the trajectory of each one can be obtained from the trajectory of the others by a symmetry transformation consisting of a rotation and a time shift (see Ref. [48]). The relative motion of vortices in the ''two plus one'' case, $\Lambda < \Lambda_c$, is distinctly different from the case $\Lambda_c < \Lambda$. Now the shape of the vortex triangle oscillates between two congruent acute isosceles triangles with different orientations, passing through the linear configuration in the midway. There is no longer any equivalence between the three vortices—one of them becomes special; it always stays in the sharp corner of the triangle, never coming as close to either of the other two as they come to each other.

The overall motion is quasiperiodic, since after one period of relative motion a vortex triangle is rotated by a certain angle $\Theta(\Lambda)$ [see Eq. (A33)], which is in general incommensurate with 2π. It is convenient to consider vortex motion in a reference frame, corotating with vortices with frequency $\Omega(\Lambda) \equiv \Theta(\Lambda)/T_{\rm rel}$. Trajectories of vortices in the corotating frame, which we denote as $\tilde{z}_m(t)$, are simply related to the laboratory frame trajectories:

$$\tilde{z}_m(t) = z_m(t) e^{-i\Omega t}, \quad m = 1,2,3. \tag{2.10}$$

They satisfy

$$\dot{\tilde{z}}_m^* = \frac{k}{2\pi i} \sum_{j \neq m} \frac{1}{\tilde{z}_m - \tilde{z}_j} + i\Omega \tilde{z}_m^*, \tag{2.11}$$

and are periodic with period $T_{\rm rel}$.

Once vortex trajectories are found, the flow field is completely specified. Its stream function is given by a sum of stream functions corresponding to individual vortices [42]:

$$\Psi(z,z^*,t) = -\frac{k}{4\pi}\sum_{m=1}^{3} \ln|z-z_m(t)|^2. \qquad (2.12)$$

The advection equation (1.2) takes the form

$$\dot{z}^* = [z^*,\Psi] = \frac{k}{2\pi i}\sum_{m=1}^{3} \frac{1}{z-z_m(t)}, \qquad (2.13)$$

where $z=x+iy$ is a complex coordinate of the tracer particle. In the corotating frame, Eq. (2.13) transforms to

$$\dot{\tilde{z}}^* = [\tilde{z}^*,\tilde{\Psi}] = \frac{k}{2\pi i}\sum_{m=1}^{3} \frac{1}{\tilde{z}-\tilde{z}_m} + i\Omega\tilde{z}^*, \qquad (2.14)$$

where $\tilde{z}=ze^{-i\Omega t}$ is the tracer coordinate in the corotating frame, and

$$\tilde{\Psi}(\tilde{z},\tilde{z}^*,t) = -\frac{k}{4\pi}\sum_{j=1}^{3} \ln|\tilde{z}-\tilde{z}_j(t)|^2 + \frac{\Omega}{2}\tilde{z}\tilde{z}^* \qquad (2.15)$$

is the stream function [Eq. (2.12)], with an additional term corresponding to rotational ''energy.'' Due to the periodicity of the vortex motion in the corotating frame, $\tilde{\Psi}$ is also periodic with period $T_{\rm rel}$, and therefore Eq. (2.14) represents a periodically forced Hamiltonian system. The character of the tracer particle motion (regular or chaotic) depends on the geometry of the vortex flow (specified by Λ), and on the initial position of the tracer relative to the vortices. The periodicity of the flow (in the corotating frame) enables us to construct a Poincaré map of tracer trajectories, and visualize the structure of the advection phase space ($\tilde{z}$ plane).

Below, we will give a brief description of the vortex motion and the resulting advection pattern for different values of Λ. We start from a ''triangular'' type of vortex geometry, $\Lambda_c<\Lambda<1$. For the lowest energy configuration, $H=0$, $\Lambda=1$, there is no relative motion—in the corotating frame vortices just stay in the vertices of equilateral triangle. Advection in this case is regular [Fig. 1(a)]. For H close to zero (Λ close to 1), vortices perform small near-circular oscillations around the vertices of the equilibrium triangle, destroying separatrices of Fig. 1(a). Two stochastic layers are formed in their place. Due to the fact that original separatrices are very close to each other, these two stochastic layers merge together for fairly small deviation of vortices from equilibrium; see Fig. 1(b). The domain of chaotic advection grows rapidly as Λ decreases; a well-developed stochastic sea already exists for $\Lambda=0.990\,656$ [Fig. 1(c)]. A typical phase portrait of the advection in the case $\Lambda>\Lambda_c$ [Fig. 1(d)] is characterized by a large connected region of chaotic motion with immersed islands where regular dynamics dominates. Three islands around the vortices (vortex cores) are easily distinguished: they have a smooth, near circular border, and are robust—they exist for any Λ. Among the near-circular *KAM* curves filling the inside area of the cores there are arcs of narrow resonant islands [Fig. 1(d)] (see Sec. V Fig. 6 for details). The other type of island, which we will refer to as an elliptic island, is as a rule irregularly shaped and extremely sensitive to the smallest variations in Λ.

The strongest chaotization occurs when Λ approaches Λ_c [Fig. 1(e)]. All elliptic islands dissolve in the stochastic sea, and the only structures remaining are vortex cores. After passing through the value $\Lambda=\Lambda_c$ the advection pattern changes abruptly due to the change of vortex motion symmetry—now one of the vortex cores is essentially larger then the other two [compare Figs. 1(e) and 1(f)]. As Λ becomes smaller, elliptic islands reappear and grow, the regular core around the isolated vortex becomes larger, and the cores around the other two vortices becomes smaller as vortices come closer to each other [Fig. 1(g)]. When Λ approaches zero, the advection pattern starts to resemble the regular advection in the field of two point vortices with strengths $k_1=k$ and $k_2=2k$ [Fig. 1(h)]. However, the region around two coalescing vortices (with linear size of order Λ) has a complex structure for any Λ: inside, there are two vortex cores separated by a thin stochastic layer from each other, and from a band of regular trajectories going around both vortices—this piece can be regarded as advection in the field of two vortices slightly perturbed by the third vortex (in particular, this perturbation is responsible for the splitting of the inner separatrix). Around it there is a transition region from scale Λ to scale L filled with a chaotic sea.

III. CASE OF STRONGLY CHAOTIC ADVECTION

Phase portraits, presented in Sec. II, show that, in the immediate neighborhood of vortices, advection is always predominantly regular—fluid around a vortex forms a coherent structure moving together with it. What determines the size of such a core? A general observation [27] is that the size of the vortex core is approximately equal to the minimum distance between the vortex and the nearest hyperbolic point of the system of streamlines, which in the case of identical vortices is about half of the minimum distance between two vortices during their motion. Chaotization of the passive particles, moving together with the core, can be achieved only by a direct ''hit'' by another core. In other words, there is no long-range chaotization; inside the cores motion is regular, apart from thin stochastic layers near the border. Why does this happen, and to what extent it is true? In this section we will answer these questions, based on an analysis of the advection in three-vortex system (2.2) in the case of ''strong chaos,'' when $\Lambda\approx\Lambda_c$.

Vortex cores are filled with regular orbits, whose shape is close to circular, so we may speak about the radius of these orbits. Let us define the radius of vortex core ζ_c as the radius of the last (most external) regular orbit in the core. Our aim is to obtain an analytical expression for ζ_c, and investigate its behavior as a function of the vortex flow parameter Λ. Consider such a core around a particular vortex numbered with $m=p$. Since we are interested in the relative motion of the tracer with respect to the vortex in the center of the core, it is convenient to consider the tracer dynamics in the reference frame moving with this vortex. To do so, we introduce the displacement of the tracer from the vortex (in the corotating frame),

$$\zeta \equiv \tilde{z}-\tilde{z}_p, \qquad (3.1)$$

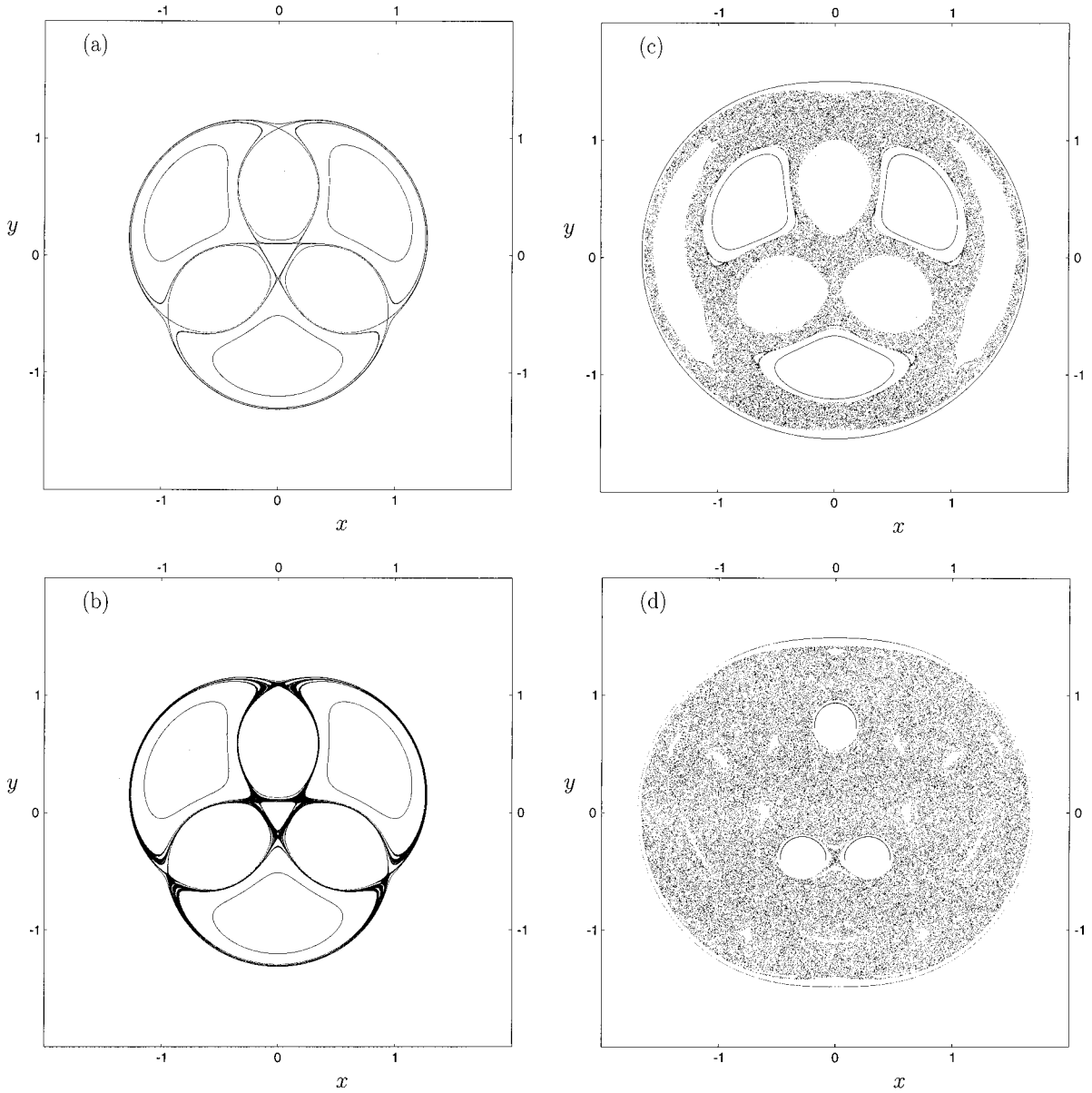

FIG. 1. Poincaré sections of passive particle trajectories: (a) Regular advection for $\Lambda=1$ (vortices form uniformly equilateral rotating triangle). (b) Destruction of separatrices and onset of chaotic advection, $\Lambda=1-9.6\times10^{-7}$. (c) $\Lambda=0.990\,656$; large mixing region already exists. (d) Typical advection pattern, $\Lambda=0.752\,192$. Arcs inside vortex cores are narrow resonant islands; see Fig. 6 for details. (e) and (f) Strong chaotization for $\Lambda\approx\Lambda_c$: (e) $\Lambda=0.707\,109>\Lambda_c$; (f) $\Lambda=0.707\,1066\,8<\Lambda_c$. (g) $\Lambda=0605\,247$; a permeable barrier separates the atmosphere around the vortex pair from the rest of the mixing region. (h) $\Lambda=0.353\,088$.

and make a canonical transformation to new coordinates using the generating function

$$F_2(\tilde{z},\zeta^*)=(\tilde{z}-\tilde{z}_p(t))\zeta^*+\tilde{z}\tilde{z}_p(t). \tag{3.2}$$

The advection equation (2.14) takes the form

$$\dot{\zeta}^*=[\zeta^*,\Phi]=\frac{k}{2\pi i}\left[\frac{1}{\zeta}+\sum_{m\neq p}\left(\frac{1}{\zeta-\tilde{z}_{mp}}+\frac{1}{\tilde{z}_{mp}}\right)\right] +i\Omega\zeta^* \quad (m=1,2,3), \tag{3.3}$$

where we have denoted the relative positions of vortices by

$$\tilde{z}_{mp}\equiv\tilde{z}_m-\tilde{z}_p\,. \tag{3.4}$$

The new stream function is

$$\Phi=\tilde{\Psi}+i/2\,\frac{\partial F_2}{\partial t} =-\frac{k}{4\pi}\left[\ln|\zeta|^2+\sum_{m\neq p}\left(\ln|\zeta-\tilde{z}_{mp}|^2+\frac{\zeta}{\tilde{z}_{mp}}+\frac{\zeta^*}{\tilde{z}^*_{mp}}\right)\right] +\frac{\Omega}{2}\,\zeta\zeta^*, \tag{3.5}$$

where we have dropped the irrelevant term depending only on time, and expressed the velocity of the vortex $\dot{\tilde{z}}_p(t)$ using Eq. (2.11).

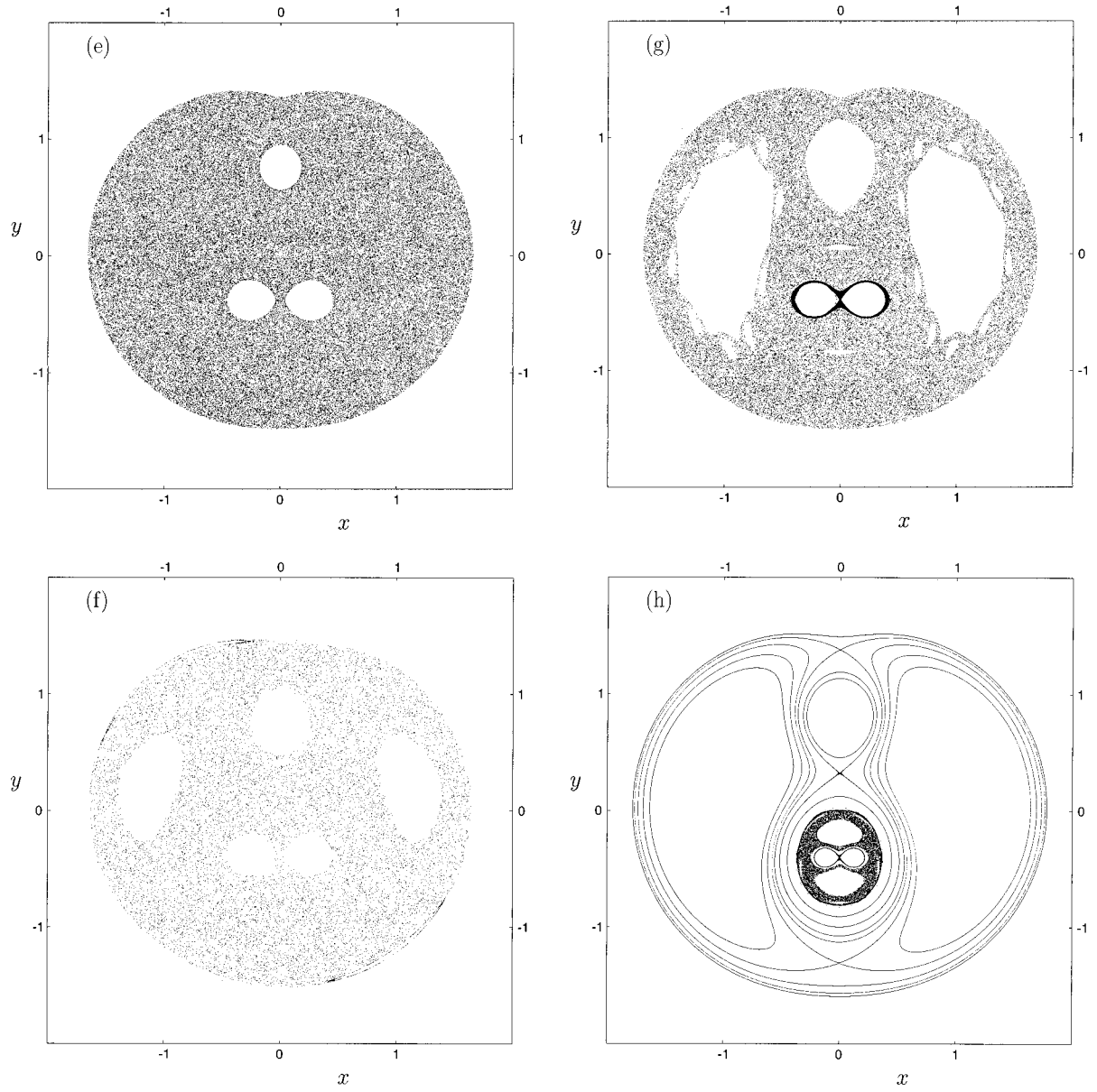

FIG. 1. (*Continued*).

The dynamics of the three-vortex system enters into Eq. (3.5). through relative vortex positions $\tilde{z}_{mp}(t)$. In the case under consideration, when $\Lambda \approx \Lambda_c$, vortices move in a typical near-separatrix fashion—they stay for a long time in the neighborhood of saddle points, periodically performing relatively fast solitonlike rearrangements (flips). Thus the vortex motion has two time scales—an interval between the flips T, which is of the order of the period of relative motion [it is equal to $T \equiv T_{\mathrm{rel}}/3$ for $\Lambda > \Lambda_c$, and $T \equiv T_{\mathrm{rel}}/2$ for $\Lambda < \Lambda_c$; see Eqs. (A27) and (A29)], and the time width of the flip t_s [see Eq. (A28)]:

$$t_s \equiv \frac{\pi}{3\sqrt{3}}, \tag{3.6}$$

where we set $k=1$ and $L=1$. As Λ approaches Λ_c, the interval between the flips grows logarithmically: $T_{\mathrm{rel}} \sim \ln|\Lambda - \Lambda_c|^{-1}$ [see Eq. (A27)], and we have

$$T \gg t_s. \tag{3.7}$$

During the time between the flips, $\tilde{z}_{mp}$ are essentially constant, and Eq. (3.5) has no explicit time dependence. This suggests the following strategy. First we introduce action-angle variables (I, ψ) for Hamiltonian (3.5), considering the vortex motion to be frozen, i.e., treating $\tilde{z}_{mp}$ as fixed parameters. Let us denote by (I_n, ψ_n) the values of the action and the angle right before the nth vortex flip. Our next step is to construct a ''flip map''

$$\hat{T}: (I_{n+1}, \psi_{n+1}) = \hat{T}(I_n, \psi_n) \tag{3.8}$$

relating the values of action-angle pair (I, ψ) before two consequitive flips. Finally, we will apply the stochasticity criterion for area-preserving maps to Eq. (3.8), and find the value of $I = I_c$ when regular trajectories around the vortex break down.

Below, we briefly outline necessary calculations, leaving some details for Appendix B. For the tracers inside the core, the distance to the center of the core $|\zeta|$ is always smaller than the distance between two vortices $|\tilde{z}_{mp}|$, and we can formally use $|\zeta/\tilde{z}_{mp}|$ as a small parameter. To indicate the real small parameter, we have to look at the time scale of the tracer motion and compare it to the vortex flip width t_s. The tracer in the core rotates with the angular frequency ω inversely proportional to the square of the distance to the vortex [see Eq. (3.15) below]. Since the tracer is much closer to the central vortex than the vortices are to each other, its rotation is fast compared to the typical vortex time t_s, and we may write, for all three time scales of the problem,

$$T \gg t_s \gg \omega^{-1}. \tag{3.9}$$

An important implication of the second inequality in Eq. (3.9) is that the time dependence of stream function (3.5) is adiabatic, since $\tilde{z}_{mp}$ vary much more slowly than the characteristic time of the tracer motion. The adiabaticity parameter

$$(\omega t_s)^{-1} \ll 1 \tag{3.10}$$

is a real small parameter of the problem.

We start by splitting stream function (3.5) into two parts (putting vortex strength $k=1$):

$$\Phi(\zeta,\zeta^*,t) = H_0(\zeta,\zeta^*) + H_1(\zeta,\zeta^*,t), \tag{3.11}$$

where H_0 is an autonomous part,

$$H_0(\zeta,\zeta^*) = -\frac{1}{4\pi}\ln|\zeta|^2 + \frac{1}{2}\,\Omega|\zeta|^2, \tag{3.12}$$

and H_1 depends on time through parameters $\tilde{z}_{mp}(t)$:

$$H_1(\zeta,\zeta^*,t) = -\frac{1}{4\pi}\sum_{m\neq p}^{3}\left(\ln|\zeta-\tilde{z}_{mp}|^2 + \frac{\zeta}{\tilde{z}_{mp}} + \frac{\zeta^*}{\tilde{z}^*_{mp}}\right). \tag{3.13}$$

Note that H_1 is of second order in $|\zeta/\tilde{z}_{mp}|$; see Eq. (B10). In the zero-order approximation we drop H_1, and consider the motion governed by the time-independent Hamiltonian (3.12). In this case solutions are circular rotations,

$$\zeta = \zeta_0 e^{i\omega t + \theta^{(0)}}, \tag{3.14}$$

with the frequency

$$\omega(J) = \frac{1}{2\pi\zeta_0^2} - \Omega = \frac{1}{4\pi|J|} - \Omega, \tag{3.15}$$

where the zeroth order action variable J is defined by

$$J = \frac{i}{8\pi}\oint(\zeta^* d\zeta - \zeta d\zeta^*) = -\frac{1}{2}\,\zeta_0^2, \tag{3.16}$$

and the zeroth order angle (which is just a polar angle in the ζ-plane) as θ:

$$\theta = \arg\,\zeta. \tag{3.17}$$

This approximation is too crude for our purpose—the effect of the other two vortices is completely neglected. To move to the next order, we rewrite stream function (3.11) in variables (J,θ) [see Eqs. (B2) and (B3)], and look for a canonical transformation to new variables $(\bar{J},\bar{\theta})$, such that dependence of Φ on $\bar{\theta}$ is eliminated in the lowest order in $|\zeta/\tilde{z}_{mp}|$. The required transformation is given by the generating function (see Appendix B)

$$S(\bar{J},\theta;t) = \bar{J}\theta + \left[\frac{1}{8\pi i\omega(J)}\sum_{m\neq p}\frac{|2\bar{J}|e^{2i\theta}}{\tilde{z}_{mp}^2} + \text{c.c.}\right], \tag{3.18}$$

where the new action $\bar{J}$ is related to the old one J by

$$\bar{J} = J + \left[\frac{1}{4\pi\omega(J)}\sum_{m\neq p}\frac{|2J|e^{2i\theta}}{\tilde{z}_{mp}^2} + \text{c.c.}\right]. \tag{3.19}$$

The generating function (3.18) depends explicitly on time through relative vortex positions $\tilde{z}_{mp}(t)$. The new Hamiltonian, describing tracer dynamics, is given by

$$\tilde{H}(\bar{J},\bar{\theta},t) = \Phi(\bar{J},\bar{\theta},t) + \frac{\partial S}{\partial t}(\bar{J},\bar{\theta},t). \tag{3.20}$$

The equation for the evolution of the adiabatic invariant follows immediately from Eqs. (3.20) and (3.18):

$$\begin{aligned}\dot{\bar{J}} &= -\frac{\partial\tilde{H}}{\partial\bar{\theta}}(\bar{J},t) = -\frac{\partial^2 S}{\partial\bar{\theta}\partial t}(\bar{J},\bar{\theta},t)\\ &= \frac{|2J|}{2\pi\omega(J)}\left[\sum_{m\neq p} e^{2i\theta}\frac{\dot{\tilde{z}}_{mp}}{\tilde{z}_{mp}^3} + \text{c.c.}\right],\end{aligned} \tag{3.21}$$

where we have replaced $\bar{\theta}$ by θ on the right-hand side with an accuracy of the first approximation.

The rate of change of $\bar{J}$ is practically zero when vortices stay near the saddle point, and the relative vortex velocities $\dot{\tilde{z}}_{mp}$ are negligible. The total change of $\bar{J}$ during the vortex flip can be evaluated by integrating right side of Eq. (3.21) through the time of the flip:

$$\Delta\bar{J}(J,\theta^{(0)}) = \int_{\Delta t}\dot{\bar{J}}dt = \frac{|2J|}{2\pi\omega(J)}\,[e^{2i\theta^{(0)}}A(J) + \text{c.c.}], \tag{3.22}$$

where

$$A(J) \equiv \int_{\Delta t} e^{2i\omega(J)t}\sum_{m\neq p}\frac{\dot{\tilde{z}}_{mp}}{\tilde{z}_{mp}^3}\,dt, \tag{3.23}$$

and the unperturbed tracer trajectory [Eq. (3.14)] is substituted under the integral. Note that we can use relative vortex positions for the separatrix vortex motion $\Lambda=\Lambda_c$ in Eq. (3.23), i.e., set $\tilde{z}_{mp}(t;\Lambda)=\tilde{z}_{mp}(t;\Lambda_c)$ and extend the integration to $\pm\infty$, since during the time of the flip they are practically indistinguishable from each other. Now we can close the contour of integration, and the integral in Eq. (3.23) will be given by the sum of contributions from singular points in the upper part of the complex plane. Due to the fast decay of the integrand up in the complex plane [ω is large; see Eq.

(3.10)], it is enough to take only the singularity, which is closest to the real axis. It turns out to be at the point

$$t_0 = i\,\frac{\pi t_s}{2} = i\,\frac{\pi^2}{6\sqrt{3}}, \tag{3.24}$$

and, for integral (3.23), we obtain

$$A(J) = A_p \omega(J) e^{-\pi\omega(J)t_s}, \tag{3.25}$$

where constants A_p, depending on the particular vortex and particular flip, were evaluated numerically:

$$|A_p| = \begin{cases} A_1 \approx 148 & \text{corner-center flip} \\ A_2 \approx 2.4 & \text{corner-corner flip;} \end{cases} \tag{3.26}$$

here the first value A_1 should be taken when the vortex under consideration stays near the central equilibrium $\tilde{z}_p = 0$ before or after the flip, and the second value A_2 when it stays outside.

The flip-map (3.8) now can be written

$$\begin{aligned} J_{n+1} &= J_n + \Delta\overline{J}(J_n, \theta_n), \\ \theta_{n+1} &= \theta_n + \omega(J_{n+1}) T(\Lambda), \end{aligned} \tag{3.27}$$

with $\Delta\overline{J}$ defined by Eq. (3.22) and $\omega(J)$ by Eq. (3.15).

To find whether a trajectory with a given initial value of J is regular or chaotic, we note that the change of the adiabatic invariant per pulse [Eq. (3.22)] is small, and the chaotization occurs mainly due to phase instability, so the stochasticity criterion can be written in a form [10]

$$K \equiv \max_{\theta \in [0,2\pi]} \left| \frac{\delta\theta_{n+1}}{\delta\theta_n} - 1 \right| > 1. \tag{3.28}$$

For the flip map (3.27), this gives

$$K = \max_{\theta \in [0,2\pi]} \left| \frac{d\omega(J)}{dJ}\, T(\Lambda)\, \frac{d\Delta\overline{J}(J_n, \theta_n)}{d\theta_n} \right| > 1. \tag{3.29}$$

From Eq. (3.22), we obtain

$$\max_{\theta \in [0,2\pi]} \left| \frac{d\Delta\overline{J}(J_n, \theta_n)}{d\theta_n} \right| = 2\,\frac{|2J|}{\pi\omega(J)}\,|A(J)|, \tag{3.30}$$

and Eqs. (3.15) and (3.16) give

$$\frac{d\omega(J)}{dJ} = \frac{1}{4\pi J^2}. \tag{3.31}$$

After substitution of Eqs. (3.30) and (3.31) into Eq. (3.29), we arrive at the following condition for the motion of the tracer to be chaotic:

$$K = \frac{|A_p| \exp(-\pi\omega(J)t_s)}{\pi^2 |J|}\, T(\Lambda) > 1. \tag{3.32}$$

To obtain the final form of Eq. (3.32), we have to substitute the frequency of the tracer rotation $\omega(J)$ from Eq. (3.15). For the frequency of overall rotation $\Omega(\Lambda)$, entering into Eq. (3.15), we can use its value at $\Lambda = \Lambda_c$, i.e., to set $\Omega(\Lambda) = \Omega(\Lambda_c) = 3/(2\pi)$. (The inaccuracy of the final result introduced by this substitution turns out to be negligible.) Thus, the tracer rotation frequency is given by

$$\omega(J) = \frac{1}{4\pi|J|} - \frac{3}{2\pi}. \tag{3.33}$$

The stochasticity criterion (3.32), rewritten in terms of the tracer orbit radius $\zeta = \sqrt{2|J|}$, takes the form

$$K = \frac{2|A_p| \exp(\pi\sqrt{3}/6)}{\pi^2 \zeta^2} \exp\left(-\frac{\pi}{6\sqrt{3}\zeta^2} \right) T(\Lambda) > 1, \tag{3.34}$$

where we have used Eqs. (3.6) and (3.33).

In the limit of small orbit radius ($\zeta \to 0$), K is exponentially small, and motion is regular no matter what the parameters of the problem are. Chaotization occurs only for the orbits with radius $\zeta > \zeta_c$, where the critical radius ζ_c (radius of the regular vortex core) is defined by

$$K(\zeta_c) = 1. \tag{3.35}$$

Using Eq. (3.34), we obtain the following equation for the radius of the vortex core:

$$\zeta_c^2 \exp\left(-\frac{\pi}{6\sqrt{3}\zeta_c^2} \right) = \frac{2|A_p| \exp(\pi\sqrt{3}/6)}{\pi^2}\, T(\Lambda). \tag{3.36}$$

Note that Eq. (3.36) has no solutions if the right-hand side is less than $C_{\min} = \pi e\sqrt{3}/18 \approx 0.82\ldots$, and there are two solutions if the right-hand side is larger than $C_{\min}$. In our case, constants A_p are fairly large [see Eq. (3.26)], and the interval between the vortex flips $T(\Lambda)$ is bounded from below by a number of order 1, so the second possibility is realized—Eq. (3.36) has two solutions. It is the smaller one that defines the vortex core radius; the larger one should be discarded, being out of range of approximations made for ζ.

The geometry of the background vortex flow enters into the equation for ζ_c only through the interval between the vortex flips $T(\Lambda)$. This dependence seems quite strong, since T diverges logarithmically when $\Lambda \to \Lambda_c$ [see Eq. (A27)]:

$$T(\Lambda) = \frac{2\pi}{3\sqrt{3}} \ln|\delta\Lambda|^{-1} + C_1 + O(|\delta\Lambda| \ln|\delta\Lambda|), \tag{3.37}$$

where we have denoted $\delta\Lambda \equiv \Lambda - \Lambda_c$. However, the exponential dependence on the left-hand side of Eq. (3.36) makes the core radius essentially independent of $T(\Lambda)$. In Fig. 2, we plot solutions of Eq. (3.36) versus the flip interval T. The solid line corresponds to the case when the vortex under consideration participates in corner-center flips, and we should take $|A_p| = A_1$ in Eq. (3.36). This happens to all three vortices in the ''triangular'' case $\Lambda > \Lambda_c$, and to the pair of vortices which are close to each other in ''two plus one'' case $\Lambda < \Lambda_c$. The dashed line gives the radius of the isolated vortex for $\Lambda < \Lambda_c$, when $|A_p| = A_2$. In the same picture we plot several ''experimental'' values of ζ_c, obtained by measuring the size of the cores in the numerically constructed Poincaré section. The error bars are due to the slightly oval

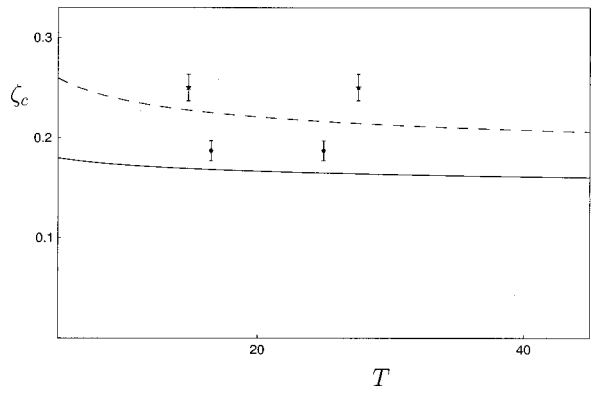

FIG. 2. Radius of the coherent core around vortices vs. interval between vortex flips $T(\Lambda)$. Dashed line—radius of the outside vortex core (only for $\Lambda<\Lambda_c$ and $m=1$) according to Eq. (3.36). Two data points for this case (stars) correspond to $\Lambda=0.707\,097\,897$, $T=14.80$ and $\Lambda=0.707\,106\,780\,96$, $T=27.60$. Solid line—radius of the vortex core in other cases [according to Eq. (3.36)]. Data points (diamonds) correspond to $\Lambda=0.707\,108\,878$, $T=16.54$ and $\Lambda=0.707\,106\,783\,15$, $T=24.97$.

shape of the real cores—the lower limiting value was taken as a minimum half-diameter of the core, and the upper as a maximum half-diameter. Experimental values agree with Eq. (3.36) up to 10% accuracy, which is the same accuracy with which the radius of the core can be defined; however, they are systematically larger as a result of the approximations being made while deriving Eq. (3.36), in particular, the use of the zeroth order adiabatic invariant [Eq. (3.16)] to define the core radius. It is possible to make corrections to Eq. (3.36) using first order adiabatic invariant (3.19) instead of Eq. (3.16); in this case the equation for the core border $\tilde{J}(J,\theta,\tilde{z}_{mp})=J_c$ describes an oval, which periodically changes its shape with time due to periodic changes of $\tilde{z}_{mp}(t)$.

Note that when T is changed from $T=5.04$ in Fig. 1(d) to $T=16.57$ in Fig. 1(e), the sizes of the cores practically do not change, while the pattern of elliptic islands becomes totally different with the smallest change in T. On the other hand, when we pass from Fig. 1(e) ($\Lambda>\Lambda_c$) to Fig. 1(f) ($\Lambda<\Lambda_c$), there is a drastic increase in the radius of one of the cores due to the change in the type of its motion.

In the limiting case $\delta\Lambda\to 0$, the right-hand side of Eq. (3.36) becomes large due to the logarithmical growth of T, and within a good approximation we can write an explicit formula for the core radius in terms of the geometrical parameter of vortex motion $\delta\Lambda$:

$$\zeta_c=\left[\frac{\pi\sqrt{3}}{18(\ln\ln|\delta\Lambda|^{-1}+\ln 4C_2)}\right]^{1/2}, \tag{3.38}$$

where

$$C_2=2|A_p|\exp(\pi\sqrt{3}/6)/\pi^2. \tag{3.39}$$

Formulas (3.36) and (3.38) indicate that the core radius should tend to zero as $\delta\Lambda\to 0$ and $T\to\infty$. Thus, in principle, regular cores around vortices can become much smaller than the half-distance between the vortices—the chaotic sea can reach any orbit with a finite radius. Nothing like this happens in practice; direct simulation of the advection equation shows no visible variation of the core size as the initial positions of vortices are taken to be closer and closer to the critical configuration [see Fig. 1(d), where $\delta\Lambda\approx 5\times 10^{-2}$; and Fig. 1(e), where $\delta\Lambda\approx 2\times 10^{-6}$]. The form of the asymptotics of ζ_c provides an explanation for this effect—ζ_c decreases extremely slowly, as $\Lambda\to\Lambda_c$ [note the double logarithm in Eq. (3.38)], and the accuracy of the simulation is insufficient to notice any significant decrease in core radius. Even machine precision calculation ($\delta\Lambda\sim 10^{-16}$, $T\approx 45$) will result in less than a 10% change of ζ_c.

The radius of the external boundary of the mixing region can be found in a similar way. The flow field, generated by vortices far from the center of vorticity, is close to that of a single point vortex of strength $3k$ located at the origin. For particles near the outer border of chaotic region, we can consider the ratio $|\tilde{z}_{mp}/\tilde{z}|$ as a small parameter. This suggests the following splitting of the stream function (2.15) into a main time-independent part and perturbation,

$$\tilde{\Psi}(\tilde{z},\tilde{z}^*,t)=H_0(\tilde{z},\tilde{z}^*)+H_1(\tilde{z},\tilde{z}^*,t), \tag{3.40}$$

with [setting $k=1$ and substituting $\Omega=\Omega(\Lambda_c)=3/2\pi$]

$$H_0(\tilde{z},\tilde{z}^*)=-\frac{3}{4\pi}\sum_{j=1}^{3}\ln|\tilde{z}|^2+\frac{3}{4\pi}|\tilde{z}|^2 \tag{3.41}$$

and

$$H_1(\tilde{z},\tilde{z}^*,t)=-\frac{1}{4\pi}\sum_{j=1}^{3}\ln|1-\tilde{z}_j(t)/\tilde{z}|^2. \tag{3.42}$$

The unperturbed part [Eq. (3.41)] describes circular rotations in the field of a point vortex of triple strength:

$$\tilde{z}(t)=Re^{i\omega(R)t+\theta^{(0)}}=\sqrt{2|J|}e^{i\omega(J)t+\theta^{(0)}}, \tag{3.43}$$

with frequency

$$\omega(J)=-\frac{3}{2\pi}(1-1/R^2)=-\frac{3}{2\pi}(1-2/|J|), \tag{3.44}$$

where action-angle variables (J,θ) are defined in a way similar to Eqs. (3.16) and (3.17):

$$J=-|\tilde{z}|^2/2,\quad \theta=\arg\tilde{z}. \tag{3.45}$$

Expanding the logarithm in Eq. (3.42) in powers of $\tilde{z}_j/\tilde{z}$, we obtain, in the lowest order,

$$\begin{aligned}H_1(\tilde{z},\tilde{z}^*,t)&=-\frac{1}{8\pi}\sum_{j=1}^{3}(\tilde{z}_j^2(t)/\tilde{z}^2+\text{c.c.})\\&=-\frac{1}{16\pi|J|}\sum_{j=1}^{3}(\tilde{z}_j^2(t)e^{-2i\theta}+\text{c.c.}).\end{aligned} \tag{3.46}$$

Note that first order terms cancel due to the conservation of the center of vorticity [Eq. (2.5)].

The dependence of the Hamiltonian on the angle variable can be eliminated by a canonical transformation to the new

variables $(\overline{J},\overline{\theta})$. The corresponding generating function $S(\overline{J},\theta;t)$ can be found from [compare to Eqs. (3.18) and (B11)]

$$\omega(\overline{J})\,\frac{\partial S}{\partial\theta}=-H_1. \tag{3.47}$$

(The averaged part of perturbation $\langle H_1\rangle=0$ in this case, and $\{H_1\}=H_1$.) The dynamics of the new action variable is given by [compare to Eq. (3.21)]

$$\dot{\overline{J}}=-\frac{\partial^2 S}{\partial\overline{\theta}\partial t}(\overline{J},\overline{\theta},t)=\frac{1}{8\pi\omega(J)|J|}\left[\sum_{j=1}^{3}e^{-2i\theta}\dot{\tilde{z}}_j\tilde{z}_j+\text{c.c.}\right], \tag{3.48}$$

where $\overline{\theta}$ is replaced by θ in the same way as in Eq. (3.21). The change of action during the vortex flip is

$$\Delta\overline{J}(J,\theta^{(0)})=\int_{\Delta t}\dot{\overline{J}}\,dt=\frac{k}{8\pi\omega(J)|J|}\,[e^{2i\theta^{(0)}}B(J)+\text{c.c.}], \tag{3.49}$$

where

$$B(J)\equiv\int_{-\infty}^{\infty}e^{-2i\omega(J)t}\left(\sum_{j=1}^{3}\dot{\tilde{z}}_j(t;\Lambda_c)\tilde{z}_j(t;\Lambda_c)\right)dt. \tag{3.50}$$

We use separatrix $(\Lambda=\Lambda_c)$ values for vortex trajectories, and extend the integration limit in Eq. (3.50) in the same manner as we did for Eq. (3.23).

In contrast with Eq. (3.23), integral (3.50) depends weakly on J if the passive particle is not too close to the origin. For such particles, the advection frequency $\omega(J)$ [in the corotating frame; see Eq. (3.44)] is close to its limiting value

$$\omega(J)\approx-\Omega=-3/2\pi, \tag{3.51}$$

and we can approximate $B(J)$ by $B(\infty)$, which is evaluated numerically:

$$B(J)\approx B\equiv\int_{-\infty}^{\infty}e^{-3it/\pi}\sum_{j=1}^{3}\dot{\tilde{z}}_j(t;\Lambda_c)\tilde{z}_j(t;\Lambda_c)dt$$
$$=0.41101\ldots\,. \tag{3.52}$$

The flip map for the far region now can be written

$$J_{n+1}=J_n+B(4\pi\omega(J)|J|)^{-1}\cos 2\theta_n,$$
$$\theta_{n+1}=\theta_n+\omega(J_{n+1})T(\Lambda), \tag{3.53}$$

where $\omega(J)$ is given by Eq. (3.44). Stochasticity criterion (3.28), applied to Eq. (3.53), gives the following equation for the boundary value of action J_c:

$$K(J_c)=\frac{BT(\Lambda)}{\pi|J_c|^3}=1. \tag{3.54}$$

The radius of the mixing region $R_{\max}\equiv\sqrt{2|J_c|}$ is equal to

$$R_{\max}=\left(\frac{4BT(\Lambda)}{\pi}\right)^{1/6}. \tag{3.55}$$

For $\Lambda\approx\Lambda_c$, a typical value of the vortex flip interval $T=16$ gives $R_{\max}=1.60$. This agrees within 10% error with the results of direct simulation; see Figs. 1(e) and 1(f). The asymptotics of Eq. (3.55) for $\Lambda\to\Lambda_c$ can be obtained, using Eq. (3.37):

$$R_{\max}=\left(\frac{8B\,\ln|\delta\Lambda|}{3\sqrt{3}}\right)^{1/6}; \tag{3.56}$$

this indicates a slow growth of the size of the mixing region as $\Lambda\to\Lambda_c$ and $T\to\infty$. This tendency is more pronounced then the asymptotic decrease of ζ_c given by Eq. (3.38), and can be verified numerically, but to a very limited extent—the value of $R_{\max}$ stays between 1.5 and 1.7, and its further increase is checked by the finite accuracy of the computation.

IV. CASE OF WEAK CHAOS, $\Lambda\approx1$

When the vortex configuration is close to one of the limiting cases $\Lambda\approx0$ or $\Lambda\approx1$, the amplitude of the vortex motion in the corotating frame is small, and the advection in the resulting flow field is predominantly regular. Below, we will consider the onset of chaotic tracer dynamics in the case $\Lambda\approx1$, when vortices perform small oscillations around the equilibrium equilateral triangular configuration (Fig. 3). The appearance of chaotic trajectories in the area around the separatrices of the integrable case $\Lambda=1$ can be demonstrated analytically [12], via the Melnikov method [35], and the width of stochastic layers, replacing destroyed separatrices, can be found using the separatrix map [41,10] (see also Ref. [49]).

Vortices are in a stable equilibrium when $\Lambda=1$; their positions in a corotating frame are constant [indeed, Eq. (A24) yields $I(t)\equiv1$, and the rest follows from Eq. (2.9)]:

$$\tilde{z}_m(t)=\frac{L}{\sqrt{3}}\,e^{-(4\pi i/3)(m-1)}\quad(m=1,2,3). \tag{4.1}$$

The stream function of the flow in the corotating frame [Eq. (2.15)] has no explicit time dependence, and is equal to

$$\tilde{\Psi}_0(\tilde{z},\tilde{z}^*)\equiv-\frac{k}{4\pi}\ln|\tilde{z}^3-\rho^3|^2+\frac{\Omega}{2}\,|\tilde{z}|^2, \tag{4.2}$$

where the frequency of the overall rotation Ω is

$$\Omega=\frac{3k}{2\pi L^2}, \tag{4.3}$$

and we have denoted by ρ the distance from vortices to the origin:

$$\rho\equiv L/\sqrt{3}. \tag{4.4}$$

Advection is regular—tracers follow the level lines of $\tilde{\Psi}_0$. Figure 3 shows singular points and separatrices of this case.

Below we consider the deviation of Λ from unity,

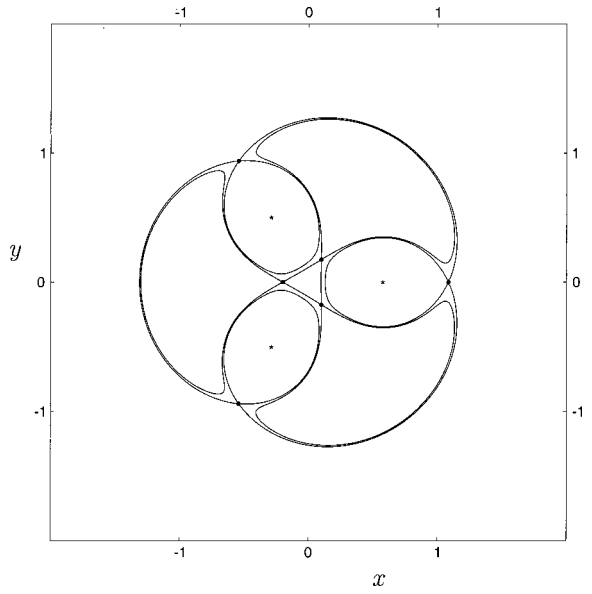

FIG. 3. Stable vortex triangle $\Lambda=1$. Separatrices of the stream function [Eq. (4.2)]. Asterisks—vortex positions [Eq. (4.1)]; solid circles—hyperbolic points [Eqs. (4.11) and (4.12)].

$$\epsilon \equiv 1-\Lambda, \tag{4.5}$$

as a small parameter, and look at the advection for the case $\epsilon \ll 1$. In the lowest order in ϵ, corrections to $\tilde{z}_m(t)$ can be found by consequitive expansion of the corresponding formulas of Appendix A (see Appendix C for details; compare to Ref. [12]):

$$\tilde{z}_m(t)=\frac{L}{\sqrt{3}}\left[e^{-(4\pi i/3)(m-1)}+\left(\frac{2\epsilon}{3}\right)^{1/2} \times e^{-(2\pi i/3)(m-1)}e^{-i\Omega t}\right], \quad m=1,2,3. \tag{4.6}$$

Up to this order the stream function of the flow in the rotating frame is:

$$\tilde{\Psi}(\tilde{z},\tilde{z}^*,t)=-\frac{k}{4\pi}\ln|\tilde{z}^3-\rho^3+(6\epsilon)^{1/2}e^{-i\Omega t}\tilde{z}\rho^2|^2 + \frac{\Omega}{2}|\tilde{z}|^2+O(\epsilon). \tag{4.7}$$

If we stay out of the immediate neighborhood of the vortices, i.e., $|\tilde{z}-\tilde{z}_m|/L \gg \sqrt{\epsilon}$, $m=1$, 2, and 3, we can expand Eq. (4.7), and rewrite it as

$$\tilde{\Psi}(\tilde{z},\tilde{z}^*,t)=\tilde{\Psi}_0(\tilde{z},\tilde{z}^*)+\epsilon^{1/2}\tilde{\Psi}_1(\tilde{z},\tilde{z}^*,t)+O(\epsilon), \tag{4.8}$$

where the autonomous part $\tilde{\Psi}_0(\tilde{z},\tilde{z}^*)$ is given by Eq. (4.2), and the perturbation is

$$\tilde{\Psi}_1(\tilde{z},\tilde{z}^*,t)\equiv-\frac{k}{4\pi}6^{1/2}\left(\frac{\tilde{z}\rho^2}{\tilde{z}^3-\rho^3}e^{-i\Omega t}+\text{c.c.}\right). \tag{4.9}$$

Equations of the tracer motion following from Eq. (4.8) are

$$\dot{\tilde{z}}^*=[\tilde{z}^*,\tilde{\Psi}]=\frac{k}{2\pi i}\frac{3\tilde{z}^2}{\tilde{z}^3-\rho^3}+i\Omega\tilde{z}^* - \frac{k}{2\pi i}(6\epsilon)^{1/2}\frac{\rho^2(\rho^3+2\tilde{z}^3)}{(\tilde{z}^3-\rho^3)^2}e^{-i\Omega t}. \tag{4.10}$$

Below we set $k=1$ and $L=1$. The unperturbed system ($\Lambda=1$, $\epsilon=0$) has two sets of three saddle points (see Fig. 3), which we denote as

$$\tilde{z}_{s,1}(m)=\frac{2}{\sqrt{3}}\cos\frac{4\pi}{9}\exp(\pi i/3+2(m-1/2)i\pi/3), \quad m=1,2,3 \tag{4.11}$$

$$\tilde{z}_{s,2}(m)=\frac{2}{\sqrt{3}}\cos\frac{\pi}{9}\exp(2(m-1)i\pi/3), \quad m=1,2,3. \tag{4.12}$$

Corresponding values of separatrix energy $\tilde{\Psi}_0$ are

$$\Psi_1^s\equiv-\frac{1}{4\pi}\ln|\tilde{z}_{s,1}^3-\rho^3|^2+\frac{3}{4\pi}|\tilde{z}_{s,1}|^2\approx 0.2681, \tag{4.13}$$

$$\Psi_2^s\equiv-\frac{1}{4\pi}\ln|\tilde{z}_{s,2}^3-\rho^3|^2+\frac{3}{4\pi}|\tilde{z}_{s,2}|^2\approx 0.2653. \tag{4.14}$$

For $\epsilon\neq 0$, near-separatrix motion becomes chaotic. To find the width of the chaotic layers, we construct the separatrix map in a usual way: we define a pair (h_n,t_n), where h_n is the deviation of the unperturbed stream function from its separatrix value,

$$h_n\equiv\tilde{\Psi}_0-\Psi_l^s, \quad l=1,2, \tag{4.15}$$

at the point when the advected particle comes closest to the saddle point in its nth passage through the saddle point neighborhood, and t_n is the moment of the center of the next velocity pulse. The dynamics of the above defined variables is governed by the mapping $\hat{T}_{\text{sep}}$: $(h_{n+1},t_{n+1})=\hat{T}_{\text{sep}}(h_n,t_n)$, which has the forms [41,10]

$$h_{n+1}=h_n+\Delta h(t_n;\sigma_n), \qquad t_{n+1}=t_n+\pi/\omega(h_{n+1}). \tag{4.16}$$

The change in energy per pulse Δh is given by the Melnikov integral

$$\Delta h(t_n;\sigma_n)\equiv\epsilon^{1/2}\int_{t_n-\infty}^{t_n+\infty}\{\tilde{\Psi}_0,\tilde{\Psi}_1\}(\tilde{z}_{\sigma_n}^{\text{sep}}(t-t_0),t)dt \tag{4.17}$$

$$=2i\epsilon^{1/2}\int_{t_n-\infty}^{t_n+\infty}\left(\frac{\partial\tilde{\Psi}_0}{\partial\tilde{z}}\frac{\partial\tilde{\Psi}_1}{\partial\tilde{z}^*}-\text{c.c.}\right) \times(\tilde{z}_{\sigma_n}^{\text{sep}}(t-t_0),t)dt, \tag{4.18}$$

where the sign variable $\sigma_n = \pm 1$ indicates on which branch the separatrix solution $\tilde{z}^{\rm sep}_{\sigma_n}(t-t_0)$ should be taken. Expressions for $\Delta h(t_n;\sigma_n)$ and $\omega(h)$ (asymptotic for small h) are derived in Appendix C [see Eqs. (C16) and (C12)]:

$$\Delta h(t_n;\sigma_n) = \frac{k}{\pi}(6\epsilon)^{1/2}\rho^2 \sin\,\Omega t_n M_{\sigma_n}, \tag{4.19}$$

$$\omega(h) \approx \frac{2\pi\lambda}{\ln|h|^{-1}}, \tag{4.20}$$

where constants λ and M_{σ_n}, evaluated numerically, are listed in Appendix C. The width of the stochastic layers is found from the equation (see Refs. [41,10])

$$\max\left|\frac{dt_{n+1}}{dt_n} - 1\right| = \max\frac{\pi}{\omega^2}\left|\frac{d\omega}{dh}\frac{d\Delta h(t_n)}{dt_n}\right| \approx 1. \tag{4.21}$$

Using Eqs. (4.19) and (4.20), we obtain the full width (both sides of separatrix) of the stochastic layer in the stream function:

$$h_{sl} = \frac{\sqrt{6}(M_+ + M_-)}{4\pi^2\lambda}\,\epsilon^{1/2}. \tag{4.22}$$

Substitution of the constants [see Eqs. (4.20), (C18), and (C19)] yields, for the first (inner) set of three saddle points,

$$h_{sl,1} = 0.33\epsilon^{1/2}; \tag{4.23}$$

and, for the second (outer),

$$h_{sl,2} = 0.29\epsilon^{1/2}. \tag{4.24}$$

The visible width of the layer, i.e., its space width on a plane, near the saddle points, is given by

$$\Delta x = |h_{sl}/\Psi''|^{1/2}, \tag{4.25}$$

where the derivative is taken along the direction transversal to the bisectrix of the angle between the separatrices. The separatrices of the system are very close to each other; see Figs. 3 and 4 and Eqs. (4.13) and (4.14); for fairly small $\epsilon = \epsilon_0 \sim 10^{-6}$, their stochastic layers merge together [see Fig. 1(b)], which puts a limit on the use of Eq. (4.22). We also have to keep in mind, that in reality the stochastic layer does not grow smoothly, but step by step, absorbing thin stochastic layers around the island chains of the resonances just outside the main layer. Figure 4(b) shows a closeup of the outer stochastic layer near the saddle point for $\epsilon = 2.4\times10^{-7}$. Its width agrees with Eq. (4.25) up to the factor 1.5.

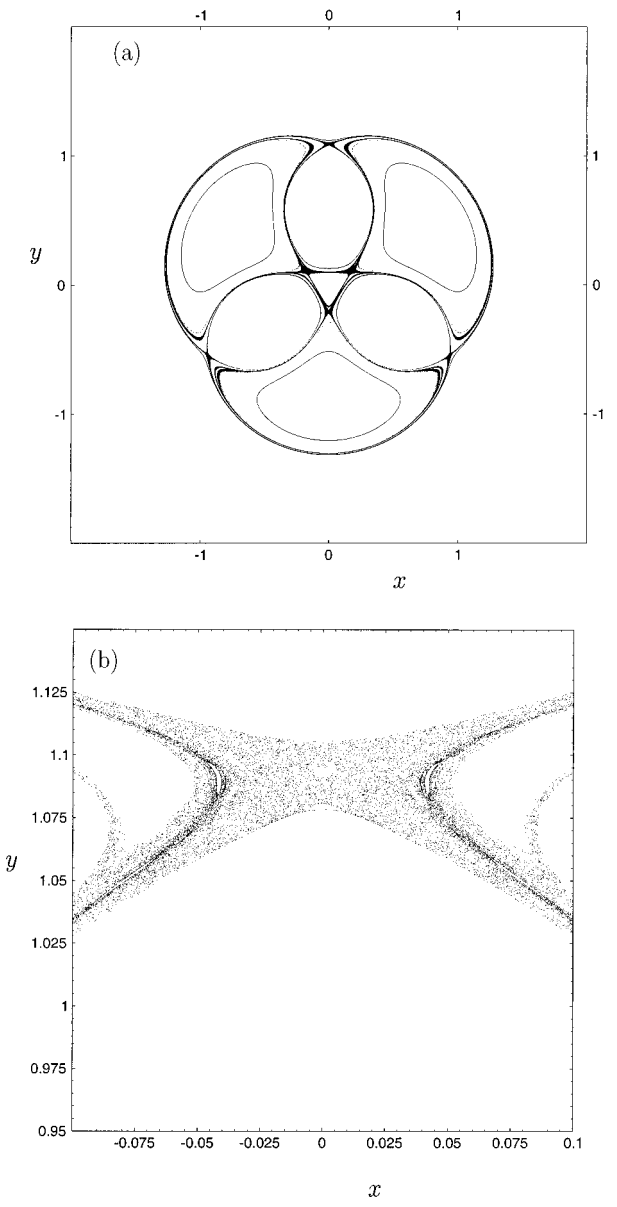

FIG. 4. (a) Stochastic layers for $\Lambda = (1-2.4)\times10^{-7}$. (b) Magnification of the area around the saddle point.

V. STRUCTURES IN THE ADVECTION PATTERN

The Hamiltonian form of advection equation (1.2) allows one to identify the coordinates of the passive particle with the canonical pair ''coordinate-momentum,'' and the flow plane can naturally be regarded as a phase space of a Hamiltonian system with $1\frac{1}{2}$ degrees of freedom. In general, the phase space of such systems is highly nonuniform, and has a multiscale hierarchy of topological structures. Roughly it can be described as domains of chaotic motion (stochastic sea) mingled with islands, inside which stable quasiperiodic motion dominates. Transport of the passive particles in the stochastic sea depends not only on such coarse characteristics of the chaotic domain as its size and general shape, but also on the fine scale formations, like singular zones around island boundaries, which may act as particle quasitraps and crucially affect all kinetic properties.

A numerically constructed Poincaré map of the tracer motion is an expedient tool for a search of fine-scale topological structures in the phase space of a Hamiltonial system with $1\frac{1}{2}$ degrees of freedom. Once it enters into a quasitrap, a trajectory has little chance to escape, so it stays there for a long time, resulting in a higher than average point density in this area of the Poincaré section (dark regions). The ergodic property would destroy this effect if the time of computation is much longer than trapping time.

We mentioned in Sec. II that the typical advection pattern of the three-point vortex system contains regular islands of

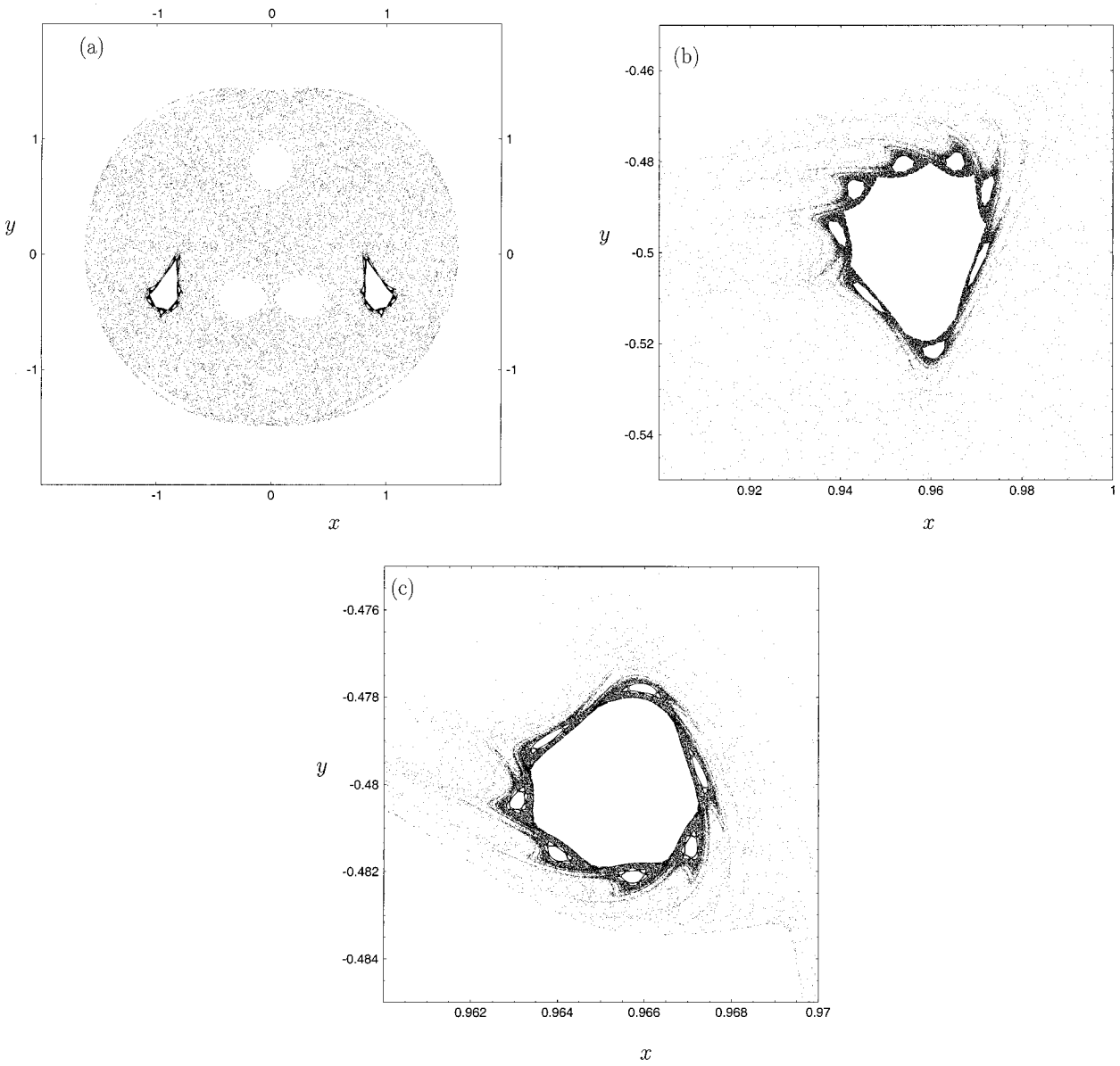

FIG. 5. (a)–(c) Hierarchy of islands for $\Lambda = 0.709\,688$.

two types. Elliptic islands vary considerably in number, size, and shape with small changes in the parameter of the background vortex flow (see Fig. 1). Their general outlook is very typical—similar kinds of structures are observed in many other cases of Hamiltonian chaos. An important feature of these objects is a singular zone around the boundary, consisting of a sticky island-around-island chain. The fractal structure of this singular zone may have a strong effect on tracer transport. Several island generations around a large elliptic island in Fig. 5(a) ($\Lambda = 0.709\,688$) are presented in Figs. 5(b) and 5(c). Dark bands around the higher order islands indicate the strong stickiness of these areas. Contrary to the elliptic islands, vortex cores are very robust. As shown in Sec. III in the range of parameter values where the strong chaotization of the tracer motion occurs, the size of these near-circular islands depends only slightly on the background flow. The inside area the cores has a structure characteristic of the phase space of a near-integrable low-dimensional Hamiltonian system—it is filled with KAM curves, and stratified with thin stochastic layers; see Fig. 6. Our simulations have shown that in certain range of values of Λ, the boundary of the cores exhibits strong stickiness (Fig. 7). A tracer particle which enters into the region of dark narrow bands around the cores in Fig. 7(a) moves coherently with the vortex for a long period of time, before being ejected back into the mixing region. These bands are not uniform; magnification of a piece of the boundary in Fig. 7(b) shows a multitude of small stretched regular subislands, embedded into the background of the chaotic motion. These subislands, in turn, have a complex structure, very sensitive to variations of the system parameters. A closeup of one of the subislands is shown in Figs. 7(c) and 7(d) for two close values of Λ.

An interesting effect is observed for $\Lambda < \Lambda_c$ when two of the vortices are somewhat isolated from the third. In this case (excluding the situation $\Lambda \approx \Lambda_c$), they form a separate structure, with a common boundary which develops from the separatrix, dividing their cores. When the third vortex is brought closer, this boundary is connected to the main stochastic sea (Fig. 8), but does not dissolve in it until the third

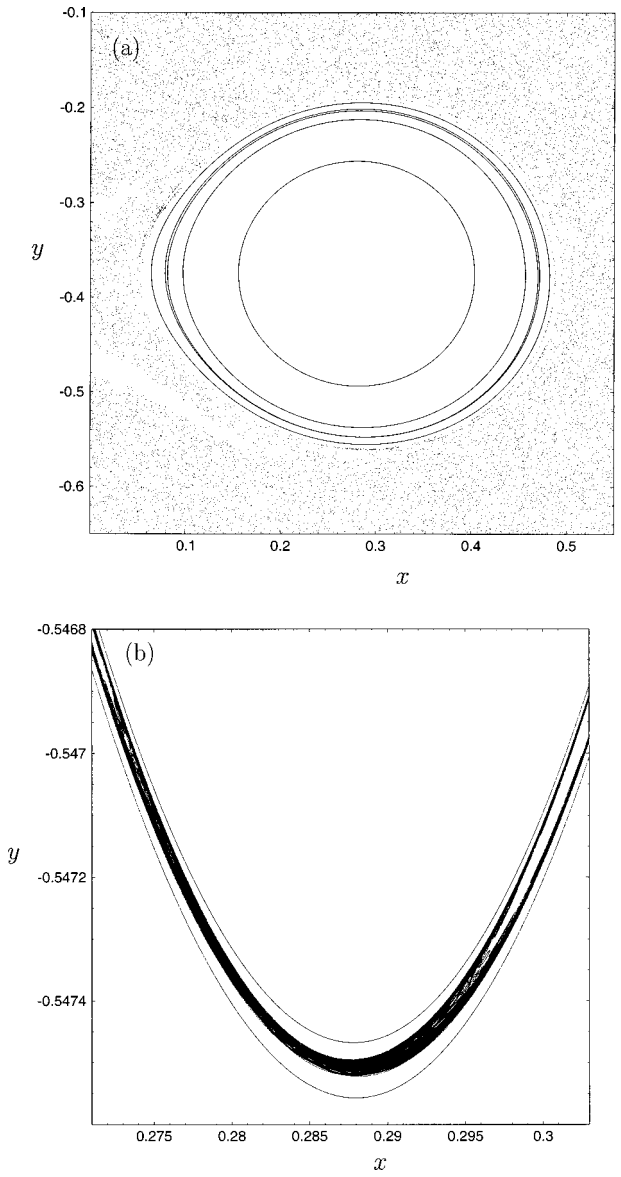

FIG. 6. (a) KAM curves inside a vortex core, $\Lambda = 0.752\,192$. The homoclinic orbit (second from outside) is in fact a narrow stochastic layer with a complex structure. (b) Magnification of the piece of this layer in the vicinity of the X point. Two close-by KAM curves are shown for contrast.

vortex is brought even closer, up to $\Lambda \approx 0.7$. This indicates that, in the multivortex system, a pair of vortices of the same sign traveling together, apart from individual cores, possess a common coherent ''atmosphere,'' and allows one to estimate how close the perturbing vortex should approach the pair in order to break it.

VI. CONCLUSION

Analysis of advection in the flow field of three identical point vortices, performed in this paper, reveals a number of features which are relevant in the case of more general 2D incompressible flows, and particularly in multivortex systems. The case of three-vortex flow is special—it is one of the simplest systems generating Lagrangian chaos. The motion of the vortices, specifying the flow, is governed by a Hamiltonian system, which turns out to be integrable due to the sufficient number of independent conservation laws. The advection equation (1.2), written in a reference frame corotating with vortices, has the structure of a periodically forced Hamiltonian system, which allows one to carry out its detailed analytical and numerical study, using a well developed methods for Hamiltonian systems with $1\frac{1}{2}$ degrees of freedom. In particular, it is possible to derive an expression for the radius of the mixing region and the radii of the regular islands around the vortices in the case of strong tracer chaotization. The formation mechanism of the vortex cores, or rather a reason for their extreme stability, is clear from the derivation: tracers inside the cores spin so rapidly that typical perturbations turn out to be adiabatic, and are averaged out. Inside the cores, tracers move in a typical pattern characteristic of a near-integrable low-dimensional Hamiltonian system—the core is filled with near circular KAM curves, narrow resonant islands, and thin stochastic layers.

Among other structures observed in the advection pattern, sticky bands around the vortex cores deserve special attention. These strong quasitraps affect transport properties of particles in the mixing region—and thus, whenever we have a regular core around vortex, we may expect an influence of its boundary on the kinetic properties. It is tempting to generalize this result for multivortex systems and other flows with coherent cores around concentrated patches of vorticity. However, the numerical construction of Poincaré sections is impossible for quasiperiodic and chaotic velocity fields, and some other method should be used for an analysis of the structure of the core boundaries in this kind of system.

ACKNOWLEDGMENTS

The authors would like to thank A. Provenzale, S. Boatto, and T. Tél for providing the results of their work prior to publication. This work was supported by the U.S. of Navy Department under Grant No. N00014-93-1-0218, and the U.S. Department of Energy under Grant No. DE-FG02-92ER54184. One of us (L.K.) would like to acknowledge the support of Margaret and Herman Sokol Travel/Research Foundation.

APPENDIX A: DYNAMICS OF THREE IDENTICAL POINT VORTICES

Below, we derive the solution of the equations of motion (2.1) of three point vortices of identical strength and polarization using the change of variables introduced in [34]. We repeat the solution for the area variable $I(t)$ [see Eq. (A17) below], presented there, and write expressions for the ''configuration angle'' $\phi_1(t)$ and ''rotation angle'' $\phi_2(t)$ [see Eqs. (A30) and (A32)], thus completely specifying the positions of vortices as functions of time [Eq. (2.9)].

Let us start from Eqs. (2.1), where we can put $k=1$ without loss of generality:

$$\dot{z}_m^* = \frac{1}{2\pi i} \sum_{j \neq m} \frac{1}{(z_m - z_j)} \quad (j,m = 1,2,3). \tag{A1}$$

Three independent integrals in involution for this system are the Hamiltonian function

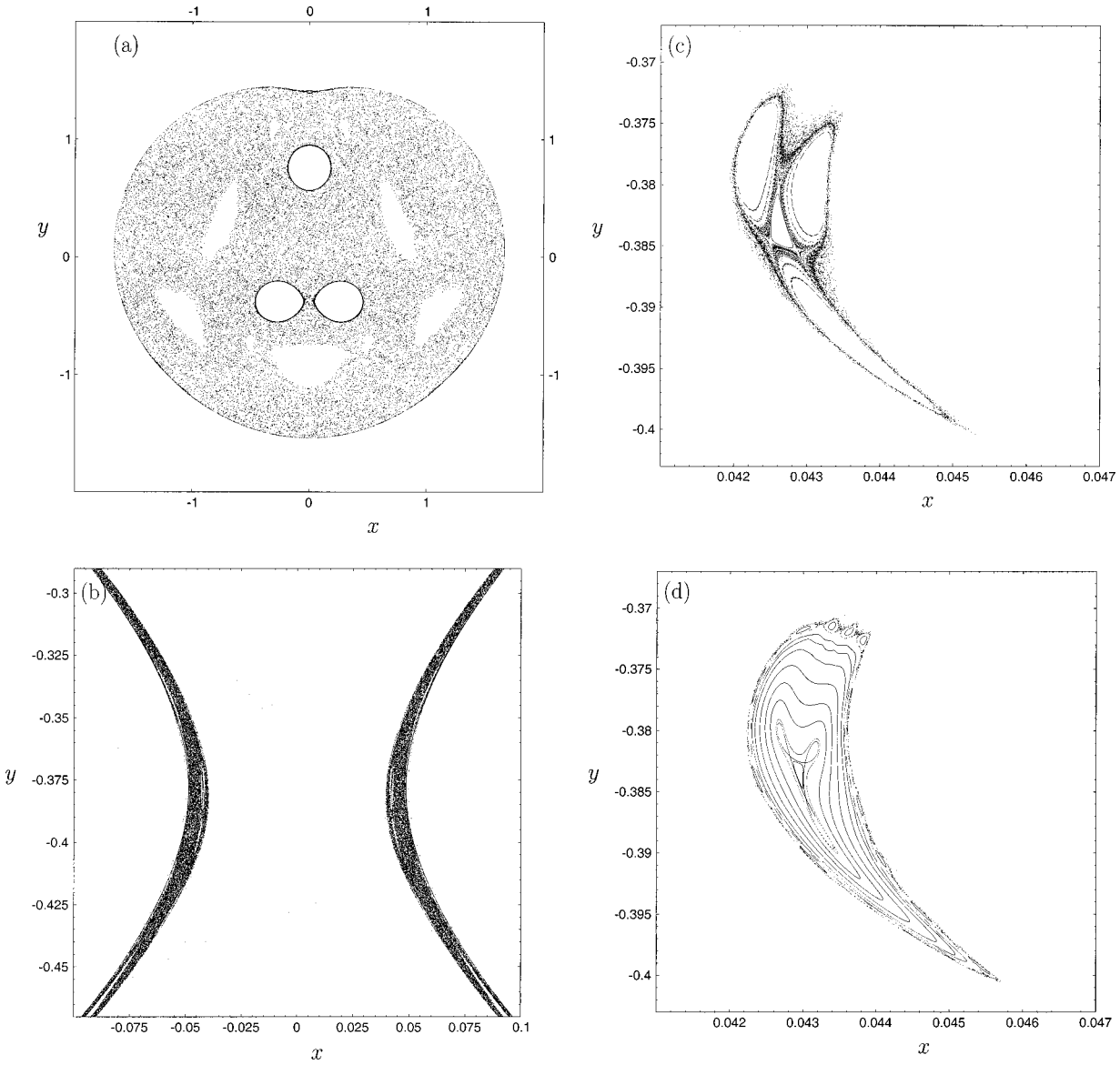

FIG. 7. (a) Stickiness of the vortex core boundaries, $\Lambda=0.716\,66$. (b) Magnification of the central part. Thin white areas inside the bands are regular island structures. Their zoom (stretched in the x direction) is shown for two close vortex geometries: (c) $\Lambda=0.716\,82$, (d) $\Lambda=0.716\,917$.

$$H=-\frac{1}{4\pi}\sum_{j\neq m}\ln|z_m-z_j|^2 \quad (j,m=1,2,3), \tag{A2}$$

and two quadratic invariants

$$Q^2+P^2=\sum_{i,j=1}^{3} z_i z_j^* \tag{A3}$$

and

$$L^2=\sum_{j=1}^{3}|z_j|^2. \tag{A4}$$

Quadratic forms Q^2+P^2 and L^2 can be simultaneously diagonalized by a discrete Fourier transform of an array of vortex positions:

$$Q_n+iP_n\equiv\frac{L}{\sqrt{3}}\sum_{j=1}^{3} e^{i(2\pi n/3)(j-1)}z_j \quad (n=0,1,2). \tag{A5}$$

Poisson brackets for new canonical variables Q_n, P_n are

$$[Q_n,P_m]=\delta_{nm}, \quad [Q_n,Q_m]=0, \quad [P_n,P_m]=0 \quad (m,n=0,1,2). \tag{A6}$$

For $n=0$, transformation (A5) shows that Q_0 and P_0 are proportional to the coordinates Q and P of the center of vorticity [Eq. (2.5)]:

$$Q_0=Q/\sqrt{3}, \quad P_0=P/\sqrt{3}, \tag{A7}$$

and are identically equal to zero, since we agreed to chose the origin of coordinates at the center of vorticity.

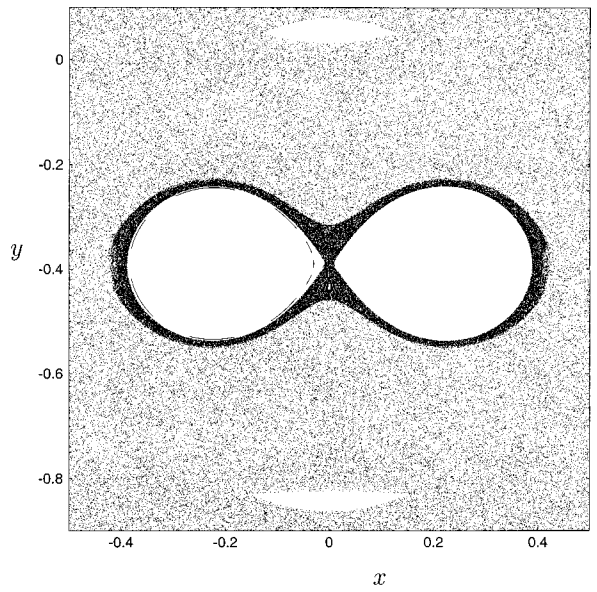

FIG. 8. $\Lambda = 0.568\,000$. The vortex pair atmosphere is a coherent structure, traveling with the pair; individual cores are wrapped by a less rigid coherent structure.

We have already reduced the number of variables to only two pairs (Q_n, P_n), $n=1$, and 2. It is convenient to use polar coordinates (J_n, θ_n) instead, defined by

$$\sqrt{2J_n}e^{i\theta_n} \equiv Q_n + iP_n \quad (n=1,2). \tag{A8}$$

Invariant (A4) is linear in J_1 and J_2:

$$L^2 = 2(J_1 + J_2). \tag{A9}$$

Vortex positions in terms of (J_n, θ_n) follow from the inverse of Eq. (A5):

$$z_j = \frac{L}{\sqrt{3}} \sum_{n=1}^{2} \sqrt{2J_n} e^{i\theta_n} e^{-2i\pi n(j-1)/3} \quad (j=1,2,3). \tag{A10}$$

The Hamiltonian function (A2), written in new variables, is

$$H = -\frac{1}{4\pi} \ln[8(J_1^3 + J_2^3 - 2(J_1 J_2)^{3/2} \cos 3(\theta_2 - \theta_1))], \tag{A11}$$

with Poisson brackets

$$[J_m, \theta_n] = \delta_{mn}, \quad [J_m, J_n] = 0, \quad [\theta_m, \theta_n] = 0 \quad (m,n=1,2). \tag{A12}$$

Since Eq. (A11) depends only on the angle difference $\phi_1 \equiv \theta_2 - \theta_1$, new canonical variables are useful:

$$\begin{aligned} I_1 &= (J_2 - J_1)/2, \quad \phi_1 \equiv \theta_2 - \theta_1, \\ I_2 &= (J_2 + J_1)/2, \quad \phi_2 \equiv \theta_2 + \theta_1. \end{aligned} \tag{A13}$$

It follows from Eq. (A9) that $I_2 = L^2/4$ is an integral of motion. Indeed, a Hamiltonian, expressed in new variables,

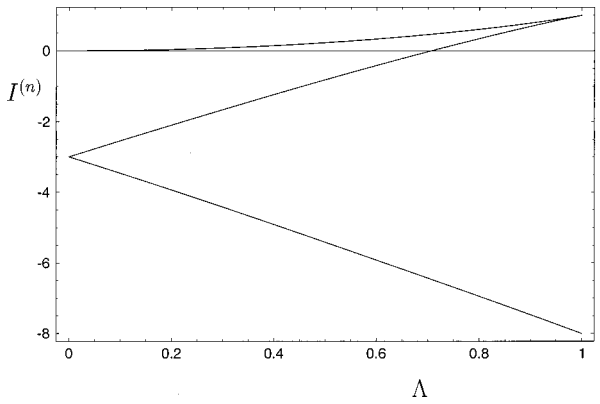

FIG. 9. Roots of the cubic [Eq. (A21)] vs Λ.

$$H = -\frac{1}{4\pi} \ln[16(I_2(I_2^2 + 3I_1^2) - (I_2^2 - I_1^2)^{3/2} \cos 3\phi_1)], \tag{A14}$$

does not depend on ϕ_2. Variable I_1 has a geometrical interpretation, which is very helpful in the analysis of the types of vortex motions. From Eqs. (A5), (A8), and (A13) it follows that

$$I_1 = \sigma A_{123}/\sqrt{3}, \tag{A15}$$

where A_{123} is the value of the area of the triangle with vertices in the current position of the point vortices (vortex triangle), and $\sigma = \pm 1$ is the orientation, which we chose to be $\sigma = +1$ for the counterclockwise arrangement of vortices, with $m=1$, 2, and 3 along the perimeter of the vortex triangle, and $\sigma = -1$ otherwise.

The equation governing the dynamics of I_1 follows from Eq. (A14):

$$\dot{I}_1 = \frac{\partial H}{\partial \phi_1} = -\frac{12e^{4\pi H}}{\pi} (I_2^2 - I_1^2)^{3/2} \sin 3\phi_1. \tag{A16}$$

The angle variable ϕ_1 can be excluded from the above equation, using the conservation of Hamiltonian (A14). It is convenient to introduce a new ''area variable''

$$I \equiv (I_1/I_2)^2 = \tfrac{16}{3} A_{123}^2/L^4, \tag{A17}$$

and use the geometrical parameter Λ defined in Eq. (2.8),

$$\Lambda = e^{-2\pi H}, \tag{A18}$$

instead of the value of the Hamiltonian H. The resulting equation for I has the form

$$\begin{aligned} \left(\frac{dI}{d\tau}\right)^2 &= -I[I^3 + 6I^2 + 3(3 - 8\Lambda^2)I + 8\Lambda^2(2\Lambda^2 - 1)] \\ &\equiv P_4(I;\Lambda) \end{aligned} \tag{A19}$$

where the rescaled time variable τ is

$$\tau = \frac{3}{2\pi\Lambda^2 L^2} t. \tag{A20}$$

The dynamics of I coincides with the motion of a particle of mass 2 in the potential $-P_4(I;\Lambda)$ with zero total energy, Eq. (A19) being a law of energy conservation.

The potential $-P_4(I;\Lambda)$ has zeros at $I=0$ and at $I=I^{(n)}$, where $I^{(n)}$ is the roots of the cubic in Eq. (A19):

$$I^{(n)}(\Lambda)=2[(1+8\Lambda^2)^{1/2}\cos(\tfrac{1}{3}(2\pi n+\delta))-1], \quad n=0,1,2, \tag{A21}$$

with

$$\cos\,\delta(\Lambda)=(-8\Lambda^4-20\Lambda^2+1)/(1+8\Lambda^2)^{3/2}. \tag{A22}$$

They are always real and satisfy $I^{(1)}<I^{(2)}<I^{(0)}$. As Λ grows from 0 to 1, the largest root $I^{(0)}$ increases from 0 to 1, $I^{(2)}$ increases from -3 to 1, and $I^{(1)}$ decreases from -3 to -8. At $\Lambda=\Lambda_c=1/\sqrt{2}$, root $I^{(2)}$ crosses zero, this value corresponds to the unstable collinear configuration $I=0$ (saddle point) and aperiodic separatrix motion (see Fig. 9).

To write the solution of Eq. (A19), we arrange the zeros of the potential in decreasing order, defining

$$J^{(0)}=I^{(0)}, \quad J^{(1)}=\max\{0,I^{(2)}\}, \qquad J^{(2)}=\min\{0,I^{(2)}\}, \quad J^{(3)}=I^{(1)}. \tag{A23}$$

Now $I(t)$ can be expressed in terms of Jacobi elliptic functions:

$$I(\tau;\Lambda)=\frac{J^{(0)}-J^{(3)}\alpha^2 sn^2(\gamma\tau)}{1-\alpha^2 sn^2(\gamma\tau)}, \tag{A24}$$

where

$$\alpha^2=(J^{(0)}-J^{(1)})/(J^{(3)}-J^{(1)}), \qquad \gamma=\tfrac{1}{2}((J^{(0)}-J^{(2)})(J^{(1)}-J^{(3)}))^{1/2}, \tag{A25}$$

and the modulus of the Jacobi elliptic function is

$$\kappa=[(J^{(0)}-J^{(1)})(J^{(2)}-J^{(3)})]/[(J^{(0)}-J^{(2)})(J^{(1)}-J^{(3)})]. \tag{A26}$$

Solution (A24) is periodic, with a period T equal to

$$T(\Lambda)=\frac{4\pi\Lambda^2L^2}{3}\frac{K(\kappa)}{\gamma}, \tag{A27}$$

where $K(k)$ is the complete elliptic integral of the first kind. During the motion, I stays between $J^{(1)}$ and $J^{(0)}$; it never reaches 0 for $\Lambda<\Lambda_c$, and does so periodically for $\Lambda>\Lambda_c$.

Case $\Lambda=\Lambda_c$ is special [$k=1$, and period (A27) has a logarithmic singularity]; there is an unstable equilibrium solution $I=0$, and a family of aperiodic solitionlike solutions given by

$$I=\left[1+\frac{2}{\sqrt{3}}\cosh(\sqrt{3}(\tau-\tau_0))\right]^{-1} =\left[1+\frac{2}{\sqrt{3}}\cosh\left(\frac{3\sqrt{3}}{2\pi L^2}(t-t_0)\right)\right]^{-1}, \tag{A28}$$

where τ_0 (or t_0) corresponds to the center of the soliton, and the scaling [Eq. (A20)] was used with $\Lambda^2=\Lambda_c^2=\frac{1}{2}$.

After one period T, the vortex triangle, repeats its shape, but the vortices are redistributed among the vertices of the triangle. It takes several periods T to return to the initial arrangement. This time defines the period of relative motion of the vortices, when the initial order of the vortices is restored, and is equal to

$$T_{\rm rel}(\Lambda)=\begin{cases}2T & \text{if } 0<\Lambda<\Lambda_c\\ 3T & \text{if } \Lambda_c<\Lambda<1.\end{cases} \tag{A29}$$

To specify the motion completely, we have to supply expressions for the angle variables ϕ_1 and ϕ_2. Conservation of H immediately yields, for the ''configuration angle'' ϕ_1,

$$\cos 3\phi_1=\frac{(1+3I)-4\Lambda^2}{(1-I)^{3/2}}. \tag{A30}$$

For the ''rotation angle'' ϕ_2, we have to go back to the Hamiltonian in the form of Eq. (A14), from which we obtain

$$\dot{\phi}_2=-\frac{\partial H}{\partial I_2}=\frac{3}{4\pi\Lambda^2L^2}\frac{4\Lambda^2-I^2-3I}{1-I}. \tag{A31}$$

Using Eq. (A19) we can rewrite this as a quadrature,

$$\phi_2(t)=\int^{I(t)}\frac{4\Lambda^2-I^2-3I}{2(1-I)\sqrt{P_4(I)}}\,dI, \tag{A32}$$

where the polynomial $P_4(I;\Lambda)$ is defined by Eq. (A19).

During one period of relative motion, the vortex triangle rotates by an angle

$$\Theta(\Lambda)=\phi_2(T_{\rm rel})-\phi_2(0), \tag{A33}$$

which can be found from Eqs. (A31) or (A32). This defines the frequency of the overall rotation of the vortex triangle:

$$\Omega(\Lambda)\equiv\Theta(\Lambda)/T_{\rm rel}=(\phi_2(T_{\rm rel})-\phi_2(0))/T_{\rm rel}. \tag{A34}$$

Performing the inverse transformation (A10), we arrive at the final expression for vortex positions in terms of constants of motion and functions $I(t)$, $\phi_1(t)$, and $\phi_2(t)$ defined by Eqs. (A24), (A30), and (A32):

$$z_m(t)=6^{-1/2}Le^{i\phi_2(t)/2}[(1-I^{1/2}(t))^{1/2}e^{-2\pi i(m-1)/3}e^{-i\phi_1(t)/2}+(1+I^{1/2}(t))^{1/2}e^{-4\pi i(m-1)/3}e^{i\phi_1(t)/2}] \quad (m=1,2,3). \tag{A35}$$

APPENDIX B: DERIVATION OF ADIABATIC INVARIANT

Here we derive the adiabatic invariant (3.19) and generating function (3.18) of the corresponding coordinate transformation. Let us start from the stream function (3.11), expressed through the zero order action-angle variables (3.16) and (3.17), considering the slow time dependence of $\tilde{z}_{\rm mp}$ to be frozen:

$$\tilde{\Psi}(J,\theta;t)=H_0(J)+\epsilon H_1(J,\theta;t), \tag{B1}$$

with $H_0(J)$ obtained from Eqs. (3.12) and (3.16),

$$H_0(J)=-\frac{1}{4\pi}\ln|2J|-\Omega J, \tag{B2}$$

and $H_1(J,\theta;t)$ from Eqs. (3.13), (3.16), and (3.17):

$$H_1(J,\theta)=-\frac{1}{4\pi}\sum_{m\neq p}\left[\ln|ie^{i\theta}\sqrt{|2J|}-\tilde{z}_{mp}|^2+\frac{ie^{i\theta}\sqrt{|2J|}}{\tilde{z}_{mp}}-\frac{ie^{-i\theta}\sqrt{|2J|}}{\tilde{z}^*_{mp}}\right]. \tag{B3}$$

A parameter ϵ in Eq. (B1) has been introduced to keep track of the order of different terms. $\epsilon=1$ in the end of the calculation.

Below we follow canonical perturbation theory (see Refs. [40,50] for details of the method). Let us look for a transformation with the generating function

$$S(\overline{J},\theta)=\overline{J}\theta+\epsilon S_1(\overline{J},\theta)+\cdots, \tag{B4}$$

such that, in new variables, the Hamiltonian

$$\tilde{H}(\overline{J};t)=\overline{H}_0(\overline{J})+\epsilon\overline{H}_1(\overline{J})+\cdots \tag{B5}$$

does not depend on the new angle up to the first order, and depends adiabatically on time through $\tilde{z}_{\rm mp}$. From Eq. (B4), we obtain a coordinate transformation

$$J=\overline{J}+\epsilon\frac{\partial S_1(\overline{J},\overline{\theta})}{\partial\overline{\theta}}+\cdots,$$

$$\theta=\overline{\theta}-\epsilon\frac{\partial S_1(\overline{J},\overline{\theta})}{\partial\overline{J}}+\cdots, \tag{B6}$$

so that Hamiltonian (B5) is

$$\tilde{H}(\overline{J};t)=H(J(\overline{J},\overline{\theta}),\theta(\vec{J},\overline{\theta}))$$

$$=H_0(\overline{J})+\epsilon H_1(\overline{J},\overline{\theta})+\epsilon\omega(\overline{J})\frac{\partial S_1}{\partial\theta}+\cdots, \tag{B7}$$

where we have used frequency (3.15):

$$\omega(\overline{J})=\frac{\partial H_0}{\partial\overline{J}}. \tag{B8}$$

Now we expand $H_1(\overline{J},\overline{\theta})$ [the second term in Eq. (B7)], defined by Eq. (B3) (we can set $\theta=\vec{\theta}$ in the first order), in Fourier series in θ, and introduce the averaged part

$$\langle H_1\rangle\equiv\frac{1}{2\pi}\int_0^{2\pi}d\overline{\theta}\,H_1(\overline{J},\overline{\theta})=-\frac{1}{4\pi}\sum_{m\neq p}\ln|\tilde{z}_{mp}|^2, \tag{B9}$$

and the oscillating part

$$\{H_1\}\equiv H_1-\langle H_1\rangle=-\frac{1}{4\pi}\sum_{m\neq p}\left[\frac{|2J|e^{2i\theta}}{\tilde{z}^2_{mp}}+\text{c.c.}\right]+\cdots, \tag{B10}$$

where the dots in the last formula remain for the higher harmonics.

Since we require, that $\overline{H}_1(\overline{J})$ in Eq. (B5) does not depend on θ, $\{H_1\}$ should be canceled by the third term in Eq. (B7), and we then have the equation for the generating function S_1:

$$\omega(\overline{J})\frac{\partial S_1}{\partial\theta}=-\{H_1\}, \tag{B11}$$

which yields Eq. (3.18):

$$S(\overline{J},\theta)=\overline{J}\theta+\left[\frac{1}{8\pi i\omega}\sum_{m\neq p}\frac{|2\overline{J}|e^{2i\theta}}{\tilde{z}^2_{mp}}+\text{c.c.}\right]. \tag{B12}$$

Substituting this in Eq. (B6), we obtain Eq. (3.19) for the first order adiabatic invariant $\overline{J}$.

APPENDIX C: CHAOTIC LAYER WIDTH FOR $\Lambda\approx 1$

As a first step to obtain the positions of the vortices up to the lowest order in ϵ [Eq. (4.6)], we expand solution (A24) of Eq. (A19) in powers of ϵ. Using Eqs. (A21), (A25), and (A26), we obtain

$$\alpha^2=-\frac{32\sqrt{2}}{81\sqrt{3}}\epsilon^{3/2}+O(\epsilon^2),\quad \gamma=3/2+O(\epsilon),$$

$$\kappa=\frac{256\sqrt{2}}{81\sqrt{3}}\epsilon^{3/2}+O(\epsilon^2), \tag{C1}$$

and, substituting Eq. (A24), obtain

$$I(t)=1-8/3\epsilon+O(\epsilon^{3/2}). \tag{C2}$$

Substituting the above expression into Eq. (A30) we find

$$\cos 3\phi_1=\cos 3\tau, \tag{C3}$$

and taking into account that $\dot{\phi}_1=-(\partial H/\partial I_1)>0$, we obtain

$$\phi_1=\tau. \tag{C4}$$

From Eq. (C2) and the expression for ϕ_2 [Eq. (A32)], it follows that, up to the irrelevant constant phase,

$$\phi_2=\tau. \tag{C5}$$

Collecting everything [see Eq. (2.9)], we obtain [Eq. (4.6)].

$$\tilde{z}_m(t)=\frac{L}{\sqrt{3}}\left(e^{-(4\pi i/3)(m-1)}+\left(\frac{2\epsilon}{3}\right)^{1/2}e^{-i\tau-(2\pi i/3)(m-1)}\right), \tag{C6}$$

where we have used definition (A20) with $\Lambda=1$.

Below we put $k=1$, and $L=1$. The asymptotic of the frequency of the near separatrix solution is defined by the motion in the neighborhood of the saddle point; in other words the period of motion is approximately equal to the time required to pass through this neighborhood. We introduce

$$\xi\equiv\tilde{z}-\tilde{z}_{s,l}, \tag{C7}$$

the distance from the saddle point, and expand stream function $\tilde{\Psi}_0$ [Eq. (4.2)] in its neighborhood [using definitions (4.3) and (4.4)]:

$$\tilde{\Psi}(\xi,\xi^*)=\Sigma_l^s+\frac{1}{4\pi}\left[\frac{\tilde{z}_s^4-2\tilde{z}_s\rho^3}{\tilde{z}_s^3-\rho^3}\frac{\xi^2}{2}+\text{c.c.}\right]+\frac{\Omega}{2}\xi\xi^*+O(\xi^3). \tag{C8}$$

This expansion can be rewritten, using definition (4.15), as

$$h=a\xi^2+2b\xi\xi^*+a^*\xi^{*2}+O(\xi^3), \tag{C9}$$

where

$$a\equiv\frac{1}{8\pi}\frac{\tilde{z}_{s,l}^4-2\tilde{z}_{s,l}\rho^3}{\tilde{z}_{s,l}^3-\rho^3},\quad b\equiv\Omega/4. \tag{C10}$$

Hamiltonian (C9) describes hyperbolic rotations with increment (decrement)

$$\lambda\equiv 4\sqrt{|a|^2-b^2}, \tag{C11}$$

and for the time to pass the saddle point we have:

$$T^{(s)}\approx-\frac{\log|h|}{\lambda}, \tag{C12}$$

which is equivalent to Eq. (4.20).

To evaluate the Melnikov integral, we use

$$\frac{\partial\tilde{\Psi}_0}{\partial\tilde{z}}=-14\pi\frac{3\tilde{z}^2}{\tilde{z}^3-\rho^3}+\frac{\Omega}{2}\tilde{z}^* \tag{C13}$$

and

$$\frac{\partial\tilde{\Psi}_1}{\partial\tilde{z}^*}=-\frac{1}{4\pi}6^{1/2}\rho^2\frac{\rho^3+2\tilde{z}^{*3}}{(\tilde{z}^{*3}-\rho^3)^2}e^{i\Omega t}. \tag{C14}$$

Substituting Eqs. (C13) and (C14) into Eq. (4.18), and shifting the integration variable, we obtain

$$\Delta h(t_n;\sigma_n)=\frac{1}{\pi}(6\epsilon)^{1/2}\rho^2\text{Im}\left[e^{-i\Omega t_n}\int_{-\infty}^{+\infty}e^{i\Omega t}\frac{\rho^3+2\tilde{z}^{*3}}{(\tilde{z}^{*3}-\rho^3)^2}\left(\frac{1}{4\pi}\frac{3\tilde{z}^2}{\tilde{z}^3-\rho^3}+\frac{\Omega}{2}\tilde{z}^*\right)dt\right]. \tag{C15}$$

In this expression $\tilde{z}^{\text{sep}}_{\sigma_n}(t)$ is a solution of the unperturbed equation (4.10) on the separatrix, centered at $t=0$. A particular branch of the separatrix is picked by $\sigma_n=\pm1$. By an appropriate rotation the separatrix solution can be made symmetric with respect to the real axis, $\tilde{z}(-t)=\tilde{z}^*(t)$, so the value of the integral in Eq. (C15) is real and we have

$$\Delta h(t_n)=\frac{1}{\pi}(6\epsilon)^{1/2}\rho^2\sin\Omega t_n M_{\sigma_n}, \tag{C16}$$

where constants M_{σ_n} are defined by the integral:

$$M_{\sigma_n}\equiv 2\,\text{Re}\int_0^{+\infty}e^{i\Omega t}\frac{\rho^3+2\tilde{z}^{*3}}{(\tilde{z}^{*3}-\rho^3)^2}\left(\frac{1}{4\pi}\frac{3\tilde{z}^2}{\tilde{z}^3-\rho^3}+\frac{\Omega}{2}\tilde{z}^*\right)dt, \tag{C17}$$

with $\tilde{z}^{\text{sep}}_{\sigma_n}(t)$ taken on the corresponding separatrix branch. Numerical evaluation of Eq. (C17) gives, for the inner separatrices

$$M_+=1.70,\quad M_-=0.560. \tag{C18}$$

and, for the outer separatrices,

$$M_+=0.537,\quad M_-=0.790. \tag{C19}$$

[1] H. Aref, J. Fluid Mech. **143**, 1 (1984).

[2] H. Aref, Philos. Trans. R. Soc. London, Ser. A **333**, 273 (1990).

[3] J. Ottino, *The Kinematics of Mixing: Stretching, Chaos, and Transport* (Cambridge University Press, Cambridge 1989).

[4] J. Ottino, Annu. Rev. Fluid Mech. **22**, 207 (1990).

[5] V. Rom-Kedar, A. Leonard and S. Wiggins, J. Fluid Mech. **214**, 347 (1990).

[6] S. Wiggins, *Chaotic Transport in Dynamical Systems* (Springer-Verlag, New York, 1992).

[7] A. Crisanti, M. Falcioni, G. Paladin, and A. Vulpiani, Nuovo Cimento **14**, 1 (1991).

[8] A. Crisanti, M. Falcioni, A. Provenzale, P. Tanga, and A. Vulpiani, Phys. Fluids A **4**, 1805 (1992).
[9] G. M. Zaslavsky, R. Z. Sagdeev, and A. A. Chernikov, Zh. Eksp. Teor. Fiz. **94**, 102 (1988) [Sov. Phys. JETP **67**, 270 (1988)].
[10] G. M. Zaslavsky, R. Z. Sagdeev, D. A. Usikov, and A. A. Chernikov, *Weak Chaos and Quasiregular Patterns* (Cambridge University Press, Cambridge, 1991).
[11] H. Aref and N. Pomphrey, Phys. Lett. A **78**, 297 (1980).
[12] S. L. Ziglin, Dokl. Akad. Nauk SSSR **250**, 1296 (1980) [Sov. Math. Dokl. **21**, 296 (1988).]
[13] Z. Neufeld and T. Tél, J. Phys. A **30**, 2263 (1997).
[14] S. Boatto and R. T. Pierrehumbert (unpublished).
[15] T. H. Solomon and J. P. Gollub, Phys. Rev. A **38**, 6280 (1988).
[16] T. H. Solomon and J. P. Gollub, Phys. Fluids **31**, 1372 (1988).
[17] V. V. Melezhko, M. Yu. Konstantinov, A. A. Gurzhi, and T. P. Konovaljuk, Phys. Fluids A **4**, 2779 (1992).
[18] L. Zanetti and P. Franzese, Eur. J. Mech. B/Fluids **12**, 43 (1993).
[19] G. Boffetta, A. Celani, and P. Franzese, J. Phys. A **29**, 3749 (1996).
[20] H. Aref and M. A. Stremler, J. Fluid Mech. **314**, 1 (1996).
[21] Á. Péntek, T. Tél, and Z. Toroczkai, J. Phys. A **28**, 2191 (1995).
[22] V. V. Meleshko, Phys. Fluids **6**, 6 (1994).
[23] G. M. Zaslavsky, M. Edelman, and B. A. Niyazov, Chaos **7**, 159 (1997).
[24] H. Aref, Annu. Rev. Fluid Mech. **15**, 345 (1983).
[25] P. G. Saffman, *Vortex Dynamics* (Cambridge University Press, Cambridge, 1992).
[26] V. V. Melezhko, and M. Yu. Konstantinov, *Dinamika Vikhrevykh Struktur* (Naukova Dumka, Kiev, 1993) (in Russian).
[27] A. Babiano, G. Boffetta, A. Provenzale, and A. Vulpiani, Phys. Fluids **6**, 2465 (1994).
[28] R. Benzi, G. Paladin, S. Patarnello, P. Santangelo, and A. Vulpiani, J. Phys. A **19**, 3771 (1986).
[29] R. Benzi, S. Patarnello, and P. Santangelo, J. Phys. A **21**, 1221 (1988).
[30] J. B. Weiss and J. C. McWilliams, Phys. Fluids A **5**, 608 (1992).
[31] D. G. Dritschel and N. J. Zabusky, Phys. Fluids **8**, 1252 (1996).
[32] E. A. Novikov and Yu. B. Sedov, Zh. Eksp. Teor. Fiz. **75**, 868 (1978) [Sov. Phys. JETP **48**, 440 (1978)].
[33] E. A. Novikov, and Yu. B. Sedov, Pis'ma Zh. Eksp. Teor. Fiz. **29**, 737 (1979) [JETP Lett. **29**, 667 (1979)].
[34] H. Aref and N. Pomphrey, Proc. R. Soc. London, Ser. A. **380**, 359 (1982).
[35] V. K. Melnikov, Trudy Moskovskogo Matem. Obschestva **12**, 3 (1963).
[36] J. C. McWilliams, J. Fluid Mech. **146**, 21 (1984).
[37] J. C. McWilliams, J. Fluid Mech. **219**, 361 (1990).
[38] D. Elhmaïdi, A. Provenzale, and A. Babiano, J. Fluid Mech. **257**, 533 (1993).
[39] G. F. Carnevale, J. C. McWilliams, Y. Pomeau, J. B. Weiss, and W. R. Young, Phys. Rev. Lett. **66**, 2735 (1991).
[40] A. J. Lichtenberg and M. A. Lieberman, *Regular and Chaotic Dynamics* (Springer-Verlag, New York, 1992).
[41] N. N. Filonenko and G. M. Zaslavsky, Zh. Eksp. Teor. Fiz. **54**, 1590 (1968) [Sov. Phys. JETP **25**, 851 (1968)].
[42] K. O. Friedrichs, *Special Topics in Fluid Dynamics* (Gordon and Breach, New York, 1966).
[43] E. A. Novikov, Zh. Eksp. Teor. Fiz. **68**, 1868 (1975) [Sov. Phys. JETP **41**, 937 (1975)].
[44] H. Aref, Phys. Fluids **22**, 393 (1979).
[45] J. L. Synge, Can. J. Math. **1**, 257 (1949).
[46] J. Tavantzis and L. Ting, Phys. Fluids **31**, 1392 (1988).
[47] A. J. Chorin and J. E. Marsden, *A Mathematical Introduction to Fluid Mechanics* (Springer-Verlag, New York, 1993).
[48] L. Kuznetsov and G. M. Zaslavsky, in *Chaos, Kinetics and Nonlinear Dynamics in Fluids and Plasmas*, edited by Sadruddin Benkadda and George M. Zaslavsky (Springer, New York, 1998).
[49] L. Kuznetsov and G. M. Zaslavsky, Phys. Rep. **288**, 457 (1997).
[50] L. D. Landau and E. M. Lifshits, *Mechanics* (Pergamon, New York, 1976).